Monthly Notices
of the
ROYAL ASTRONOMICAL SOCIETY

MNRAS **466,** 1903–1924 (2017)
Advance Access publication 2016 December 12

doi:10.1093/mnras/stw3209

# The SILCC project – III. Regulation of star formation and outflows by stellar winds and supernovae

Andrea Gatto,[1] Stefanie Walch,[2]★ Thorsten Naab,[1]★ Philipp Girichidis,[1] Richard Wünsch,[3] Simon C. O. Glover,[4] Ralf S. Klessen,[4,5] Paul C. Clark,[6] Thomas Peters,[1] Dominik Derigs,[2] Christian Baczynski[4] and Joachim Puls[7]

[1]*Max-Planck-Institut für Astrophysik, Karl-Schwarzschild Strasse 1, D-85748 Garching, Germany*
[2]*I. Physikalisches Institut, Universität Köln, Zülpicher Strasse 77, D-50937 Köln, Germany*
[3]*Astronomický Ústav, Akademie věd česky Republiky, Boční II 1401, CZ-14131 Praha, Czech Republic*
[4]*Universität Heidelberg, Zentrum für Astronomie, Institut für Theoretische Astrophysik, Albert-Ueberle-Str. 2, D-69120 Heidelberg, Germany*
[5]*Universität Heidelberg, Interdisziplinäres Zentrum für WIssenschaftliches Rechnen (IWR), D-69120 Heidelberg, Germany*
[6]*School of Physics and Astronomy, Cardiff University, 5 The Parade, Cardiff CF24 3AA, UK*
[7]*LMU Munich, Universitäts-Sternwarte, Scheinerstrasse 1, D-81679 München, Germany*

Accepted 2016 December 7. Received 2016 December 2; in original form 2016 May 9

## ABSTRACT

We study the impact of stellar winds and supernovae on the multiphase interstellar medium using three-dimensional hydrodynamical simulations carried out with FLASH. The selected galactic disc region has a size of $(500\,\mathrm{pc})^2 \times \pm 5\,\mathrm{kpc}$ and a gas surface density of $10\,\mathrm{M}_\odot\,\mathrm{pc}^{-2}$. The simulations include an external stellar potential and gas self-gravity, radiative cooling and diffuse heating, sink particles representing star clusters, stellar winds from these clusters that combine the winds from individual massive stars by following their evolution tracks, and subsequent supernova explosions. Dust and gas (self-) shielding is followed to compute the chemical state of the gas with a chemical network. We find that stellar winds can regulate star (cluster) formation. Since the winds suppress the accretion of fresh gas soon after the cluster has formed, they lead to clusters that have lower average masses ($10^2$–$10^{4.3}\,\mathrm{M}_\odot$) and form on shorter time-scales ($10^{-3}$–10 Myr). In particular, we find an anticorrelation of cluster mass and accretion time-scale. Without winds, the star clusters easily grow to larger masses for ∼5 Myr until the first supernova explodes. Overall, the most massive stars provide the most wind energy input, while objects beginning their evolution as B-type stars contribute most of the supernova energy input. A significant outflow from the disc (mass loading $\gtrsim$1 at 1 kpc) can be launched by thermal gas pressure if more than 50 per cent of the volume near the disc mid-plane can be heated to $T > 3 \times 10^5$ K. Stellar winds alone cannot create a hot volume-filling phase. The models that are in best agreement with observed star formation rates drive either no outflows or weak outflows.

**Key words:** methods: numerical – ISM: evolution – ISM: structure – galaxies: ISM.

## 1 INTRODUCTION

The life cycle of the interstellar medium (ISM) is tightly connected with the star formation activity of a galaxy. Cold and dense molecular gas can partly undergo gravitational collapse leading to star formation. Eventually, newly formed massive stars (with mass $>8\,\mathrm{M}_\odot$) strongly impact the surrounding ISM by ionizing radiation (e.g. Peters et al. 2010, 2011; Dale, Ercolano & Bonnell 2012; Walch et al. 2012, 2013; Dale et al. 2014; Geen et al. 2015), radiation pressure (e.g. Krumholz & Matzner 2009; Murray, Quataert & Thompson 2010; Krumholz & Thompson 2012), stellar winds (e.g. Wünsch et al. 2008, 2011; Pellegrini, Baldwin & Ferland 2011; Toalá & Arthur 2011; Dale, Ercolano & Bonnell 2012; Rogers & Pittard 2013; Mackey et al. 2015; Klassen et al. 2016), and supernova (SN) explosions (e.g. Mac Low et al. 2005; Dib, Bell & Burkert 2006; Gatto et al. 2015; Iffrig & Hennebelle 2015; Li et al. 2015; Martizzi, Faucher-Giguère & Quataert 2015; Walch & Naab 2015; Haid et al. 2016). These processes – termed 'feedback' in astrophysical slang – locally

★ E-mail: walch@ph1.uni-koeln.de (SW); naab@mpa-garching.mpg.de (TN)

© 2016 The Authors
Published by Oxford University Press on behalf of the Royal Astronomical Society

heat and disperse the surrounding ISM, but may also compress some fraction of the gas and trigger the formation of new stars.

Stellar feedback may drive supersonic turbulent motions in the ISM gas (see e.g. Klessen & Glover 2016). As an example, observations of broad H and textscCO emission lines show that warm, cold, and molecular gas are shaped by supersonic turbulent motions with a typical velocity dispersion from few to $\approx$10 km s$^{-1}$ (Larson 1981; Goodman et al. 1998; Heiles & Troland 2003; Petric & Rupen 2007; Tamburro et al. 2009; Caldú-Primo et al. 2013; Ianjamasimanana et al. 2015).

Further, it has been proposed that feedback from (massive) stars can locally limit the fraction of gas mass that is converted into stars, i.e. the star formation efficiency, $\epsilon_{\rm SF}$. In the Milky Way, star formation is inefficient with $\epsilon_{\rm SF} \sim 1$ per cent (Zuckerman & Evans 1974; Mac Low & Klessen 2004). The inefficiency of star formation has been confirmed for a large number of star-forming galaxies at local and high redshifts $z \approx 0$–2 (Leroy et al. 2008; Genzel et al. 2010; Tacconi et al. 2013). The importance of stellar feedback for the regulation of star formation relative to other processes, such as large-scale shear flows around spiral arms (Dobbs & Pringle 2013), is still a matter of debate.

Stellar feedback influences the thermal and kinetic pressures of the gas at larger scales (Ostriker, McKee & Leroy 2010; Girichidis et al. 2016a). In particular, SN explosions can create a hot ionized medium (Cox & Smith 1974; McKee & Ostriker 1977) with high volume-filling factors (Ferrière 2001; Kalberla & Dedes 2008; Walch et al. 2015), which may launch powerful outflows from galactic discs (e.g. Oppenheimer et al. 2010; Creasey, Theuns & Bower 2013; Hopkins et al. 2014; Marinacci et al. 2014; Peters et al. 2015; Girichidis et al. 2016a). Galactic outflows remove gas that would otherwise be available for star formation and hence might regulate galaxy evolution on global scales. In this context, the fundamental role of massive stars for the evolution of star-forming galaxies with a large range of masses has been emphasized in many recent numerical studies (see e.g. Agertz et al. 2013; Hopkins et al. 2014; Somerville & Davé 2015). These simulations test different feedback processes, but suffer from limited spatial and/or mass resolution and thus, cannot capture many physical processes regulating the ISM on small and intermediate scales.

To understand the non-linear interaction between the interstellar matter and the young stellar population and to investigate the multitude of the relevant physical processes, many authors have carried out studies of the ISM in representative pieces of isolated, stratified, galactic discs using (magneto-)hydrodynamic (MHD) simulations. They investigate the structure of the ISM that is stirred by SN feedback (e.g. de Avillez & Breitschwerdt 2004, 2007; Joung & Mac Low 2006; Joung, Mac Low & Bryan 2009; Hill et al. 2012; Shetty & Ostriker 2012; Kim, Ostriker & Kim 2013), with self-gravity (Gent et al. 2013a,b; Hennebelle & Iffrig 2014; Kim & Ostriker 2015b), and e.g. with different cooling functions (Gent et al. 2013b).

In Walch et al. (2015, hereafter Paper I), we demonstrated how the positioning of SN explosions relative to the cold and dense gas in the disc affects the multiphase temperature (from $\sim$10 to $10^8$K) and chemical structure ($H_2$, H, $H^+$) of the ISM. With a fixed SN rate, which is informed by the Kennicutt–Schmidt (KS; Kennicutt 1998) relation and connecting the gas surface density to a SN rate using a standard initial mass function (IMF; e.g. Kroupa 2002; Chabrier 2003), we evolved the simulation using MHD, gas self-gravity, a chemical network, and radiative transfer of diffuse radiation to model the formation of molecular gas in the form of $H_2$ and CO. We showed that SNe located at random positions lead to a bubbly ISM with a high volume-filling fraction (VFF) of hot gas on the one hand, and at the same time help self-gravity to drive the formation of $H_2$ in filaments and clumps. In these runs, the thermal feedback is strong enough to launch galactic fountain flows that have a multiphase structure (see Girichidis et al. 2016a, hereafter Paper II). SNe that explode within dense gas have a low heating efficiency and produce low $H_2$ mass fractions. In the case where all SNe are associated with dense gas, we obtained a very low VFF of hot gas (see also Gatto et al. 2015) and there were no outflows from the disc. However, these proofs of concept studies lack a direct connection between dense gas and the formation of new stars.

A recent study by Hennebelle & Iffrig (2014), uses sink particles to more self-consistently model the star formation in such a stratified galactic disc (see also Slyz et al. 2005, for similar work using a periodic box). Their SN rate is not fixed but correlated in space and time with the sink particle positions and accretion rate. The energy from SN explosions is injected right after the formation of each massive star (see also e.g. Kim et al. 2013; Kim & Ostriker 2015b), thus neglecting the time delay of the explosions corresponding to the stellar lifetime of single stars (typically 5–40 Myr). They show that instantaneous SN feedback can significantly lower the star formation rate (SFR) by a factor of 20–30. A complication in this context is that it remains unclear whether in a more realistic set-up the SN explosions remain the SFR limiting factor when other pre-SN feedback processes and realistic SN delay time distributions are assumed.

In this paper, we improve on earlier studies (Papers I and II) by studying the mutual influence of the three-phase ISM, self-consistent star formation, and feedback from massive stars in the form of stellar winds and SNe with realistic delay time distributions. The feedback is associated with accreting sink particles that represent young star clusters. We follow the evolution of each single massive star using the latest Geneva stellar evolution tracks by Ekström et al. (2012) and study the relative impact of stellar winds and SNe on the structure of the ISM, the SFR, and the onset of galactic outflows. We will argue that the inclusion of stellar winds (and possibly other pre-SN injection processes of massive stars not investigated here, like ionizing radiation and radiation pressure) qualitatively change the timing and the regulation mechanisms for star-cluster formation.

The manuscript is organized as follows: in Section 2, we describe our model and we list the important parameters and simulations. In Section 3, we present our qualitative results, with a more detailed discussion on the wind and SN feedback regulation processes in Section 4. The effects on disc outflows are presented in Section 5, and we conclude in Section 6.

## 2 NUMERICAL METHOD

We use the Eulerian, adaptive mesh refinement, MHD code FLASH 4 (Fryxell et al. 2000; Dubey et al. 2008, 2013) with the directionally split, Bouchut HLL5R solver (Bouchut, Klingenberg & Waagan 2007, 2010; Waagan 2009; Waagan, Federrath & Klingenberg 2011) to simulate the ISM in a stratified disc. The size of the vertically elongated box is 500 pc $\times$ 500 pc $\times \pm$ 5 kpc. We set periodic boundary conditions in $x$- and $y$-direction and use outflow boundary conditions in the $z$-direction. Near the disc mid-plane the resolution is $\Delta x \simeq 3.9$ pc, and above and below $z = 1$ kpc we use $\Delta x \simeq 7.8$ pc. We solve the ideal MHD equations and additionally include

(i) a static potential to model the old stellar component in the disc (Section 2.1),
(ii) gas self-gravity (Section 2.1),
(iii) radiative cooling and diffuse heating by a smooth interstellar radiation field (ISRF) with $G_0 = 1.7$ (Section 2.2),
(iv) dust and gas (self-) shielding (Section 2.2),
(v) a chemical network to explicitly follow H, $H^+$, $H_2$, CO, $C^+$ (Section 2.2),
(vi) star-cluster-sink particles (Section 2.3) with a sub-grid prescription that models the formation and evolution of the massive stars in the star cluster using stellar tracks (Section 2.4), and
(vii) stellar winds and/or SN feedback from the star-cluster-sink particles (Section 2.4).

In this paper, we do not include the impact of ionizing radiation from the massive stars on the ISM. We also do not include galactic shear unlike e.g. Kim & Ostriker (2015b), but for our particular set-up the influence of shear is probably negligible (see section 7.4 in Paper II for an estimate of the Rossby number). Below, we briefly describe our numerical method, but also refer to Paper I for more details.

### 2.1 Gravity

Three terms contribute to the gravitational acceleration of the gas: self-gravity, the static background potential caused by old stars in the disc, and newly forming sink particles:

$$\boldsymbol{g} = \boldsymbol{g}_{\rm sg} + \boldsymbol{g}_{\rm ext} + \boldsymbol{g}_{\rm sinks}. \quad (1)$$

The gravitational acceleration due to self-gravity, $\boldsymbol{g}_{\rm sg}$, is computed by solving Poisson's equation for the gas in three dimensions using a tree-based method described in detail in Paper I and Wünsch et al. (in preparation).

We neglect dark matter but consider the external potential generated by the old stellar component in the galactic disc, which we assume to follow the distribution (Spitzer 1942)

$$\rho_*(z) = \rho_*(0)\,\mathrm{sech}^2(z/2z_{\rm d})\,, \quad (2)$$

where $\rho_*$ is the density of stars at height $z$. We take $\rho_*(0) = 0.075\,\mathrm{M_\odot\,pc^{-3}}$, which corresponds to a total stellar surface density of $30\,\mathrm{M_\odot\,pc^{-2}}$ with a scaleheight $z_{\rm d} = 100\,\mathrm{pc}$. We then integrate the one-dimensional Poisson equation along the $z$-direction for $\rho_*$ to get the external acceleration: $\boldsymbol{g}_{\rm ext}(z)$.

The contribution of sink particles to the gravitational acceleration of the gas, $\boldsymbol{g}_{\rm sinks}$, is taken into account. Following Federrath et al. (2010), outside the accretion radius (see Section 2.3) this involves a direct summation for all computational cells and all particles. Within the accretion radius, a cubic spline gravitational softening scheme is applied to avoid diverging accelerations at close distances. The sink particles are advanced using a Leapfrog time integration scheme with sub-cycling. The according forces are computed from particle–particle as well as gas–particle interaction (for more details see Federrath et al. 2010). In addition, we include the force due to the external gravitational potential.

### 2.2 Cooling, heating, and chemistry

We include heating and cooling processes using a simplified chemical network based on Glover & Mac Low (2007a,b) and Nelson & Langer (1997) to follow the abundances of seven chemical species: H, $H^+$, $H_2$, CO, and $C^+$, as well as free electrons and atomic oxygen, which are tracked utilizing conservation laws. The rate equations for $H_2$ and CO include the effect of dust shielding and molecular (self-) shielding (Glover et al. 2010). The total, $H_2$, and CO column densities, which are necessary to compute the shielding coefficients, are estimated using the TREECOL algorithm of Clark, Glover & Klessen (2012), which we implemented into FLASH 4. For further details, see Paper I and Wünsch et al. (in preparation).

Cooling of gas with $T > 10^4$ K is modelled with the cooling rates of Gnat & Ferland (2012), which assumes collisional ionization equilibrium. For lower temperatures, non-equilibrium cooling rates for the respective chemical abundances, as well as heating by the photoelectric effect, cosmic rays, X-rays, and UV radiation from a diffuse ISRF with $G_0 = 1.7$ (Habing 1968; Draine 1978), are included (Glover et al. 2010; Glover & Clark 2012). We assume a cosmic ray ionization rate of $\zeta = 3 \times 10^{-17}\mathrm{s^{-1}}$, and X-ray ionization and heating rates based onWolfire et al. (1995). For simplicity, we assume that the ISRF is constant everywhere in the computational domain. However, it is attenuated in shielded regions, where the shielding depends on the column densities (total, $H_2$, and CO), which are determined through TREECOL.

For all simulations, the gas has solar metallicity with abundances $x_{\rm O,\,tot} = 3.16 \times 10^{-4}$, $x_{\rm Si^+} = 1.5 \times 10^{-5}$, and $x_{\rm C,\,tot} = 1.41 \times 10^{-4}$ (Sembach et al. 2000). The (constant) dust-to-gas mass ratio is set to $10^{-2}$. For further details, we refer the reader to Paper I.

### 2.3 Sink particles

We include the sink particles unit from the FLASH 4 public release, described in Federrath et al. (2010, see also Bate, Bonnell & Price 1995; Krumholz, McKee & Klein 2004; Jappsen et al. 2005; Hubber, Walch & Whitworth 2013; Bleuler & Teyssier 2014 for details on the implementation of sink particles in other Smoothed Particle Hydrodynamics and Eulerian codes). In our models, collisionless sink particles provide the framework to model the formation of internally unresolved star clusters in dense regions undergoing gravitational collapse. Following Federrath et al. (2010), a sink particle is created in a particular cell if

(i) the gas density is higher than a user-defined density threshold $\rho_{\rm sink}$,
(ii) all cells within the accretion radius, $r_{\rm accr}$, are at the highest refinement level,
(iii) the cell represents a local gravitational potential minimum,
(iv) the gas within $r_{\rm accr}$ is Jeans unstable,
(v) the gas within $r_{\rm accr}$ is in a converging flow ($\nabla \cdot \boldsymbol{v} < 0$),
(vi) the gas within $r_{\rm accr}$ is gravitationally bound, and
(vii) the sink's accretion radius does not overlap with that of another existing sink.

Once a sink particle is formed, it can accrete gas within $r_{\rm accr}$ if the gas density exceeds $\rho_{\rm sink}$. Additional checks are performed to ensure that only bound, collapsing gas is removed from the grid and added to the sink. We set the accretion radius to $r_{\rm accr} = 4 \times \Delta x = 15.6\,\mathrm{pc}$, where $\Delta x = 3.9$ pc is the cell size at the maximum refinement level (a typical value; see e.g. Krumholz et al. 2004; Hennebelle & Iffrig 2014). This satisfies the Truelove criterion (Truelove et al. 1997) and the more stringent criterion of isothermal MHD collapse found by Heitsch, Mac Low & Klessen (2001). The choice of $r_{\rm accr}$ determines $\rho_{\rm sink}$, below which the gas can be considered Jeans-stable. Then, we have

$$\lambda_{\rm J} = \left(\frac{\pi c_{\rm s}^2}{G\rho_{\rm sink}}\right)^{\frac{1}{2}} = 2 \times r_{\rm accr} \approx 31.2\,\mathrm{pc}\,, \quad (3)$$

with $c_s = (k_B T/m_p)^{1/2}$ the isothermal sound speed of monoatomic gas. This gives

$$\rho_{sink} = \frac{\pi k_B}{m_p G} \frac{T}{(2 \times r_{accr})^2} . \quad (4)$$

For a temperature of $T = 300$ K, below which we consider the gas to be in the thermally stable, cold phase, the density threshold is $\rho_{sink} \approx 1.26 \times 10^{-22}$ g cm$^{-3}$ (this is an order of magnitude lower than the sink density threshold used by Hennebelle & Iffrig 2014). Often, we find even lower temperatures in the dense gas (down to 10 K), for which the Jeans length cannot be resolved with our choice of $r_{accr}$. However, we do not consider this to be a severe problem since the sink particles in our simulations do not represent individual stars, but are rather considered to be tracing star clusters with an internal stellar IMF (see Section 2.4). Therefore, we do not need to resolve the fragmentation limit with $\rho_{sink}$, but rather treat it as a free parameter. We present simulations with different sink formation thresholds, ranging from $\rho_{sink} = 2 \times 10^{-22}$ g cm$^{-3}$ or a particle density of $n_{sink} \approx 10^2$ cm$^{-3}$ to $\rho_{sink} = 2 \times 10^{-20}$ g cm$^{-3}$ or $n_{sink} \approx 10^4$ cm$^{-3}$.

### 2.4 Sub-grid model for cluster-sink particles

The sink particles formed in our simulations have masses of $M_{sink} \sim 10^2$–$10^{5.3}$ M$_\odot$, i.e. they are groups of stars (star clusters). We therefore call them *cluster-sink particles* and implement a sub-grid model to follow the evolution of massive stars that are supposedly forming within them.

We assume that all gas accreted on to a sink is converted into stars, which corresponds to a *cluster formation efficiency* of 100 per cent. This choice is numerically motivated and prevents gas from being artificially locked up inside the sink without the possibility to be heated or dispersed by stellar feedback or to eventually collapse into stars. We note that the *cluster formation efficiency* is a theoretical concept and is not equal to the *star formation efficiency*. The latter needs to be computed from the ratio of the SFR and the available mass in atomic and/or molecular hydrogen (as indicated when comparing our simulation results with recent observations in Fig. 8).

Massive star content: all of $M_{sink}$ is available for star formation. We are only interested in following the evolution of individual massive stars that have significant stellar winds and explode as SNe (that is stars with mass >8 M$_\odot$). Therefore, we have implemented the following model.

(i) One massive star is created for every 120 M$_\odot$ of gas that is converted into or accreted on to a sink particle (star cluster).

(ii) The mass of every new-born star is randomly sampled from the Salpeter IMF (Salpeter 1955) within a mass range of 9–120 M$_\odot$.

(iii) The rest of the mass is assumed to reside in low-mass stars, which are not followed individually.

(iv) Not every massive star is created upon sink formation. Whenever enough mass (a mass unit of 120 M$_\odot$) becomes available (it has been accumulated by gas accretion on to the sink), a new massive star is spawned.

(v) The number of massive stars within each sink, $N_\star$, is different for each sink and changes as a function of time.

Stellar wind model: the evolution of each massive star is followed using the latest Geneva stellar evolution tracks from the zero-age main sequence (ZAMS) to the Wolf–Rayet (WR)/pre-SN phase by Ekström et al. (2012). We interpolate and store 112 tracks (for stars with 9–120 M$_\odot$, separated by 1 M$_\odot$). We do not take into account a delay time due to star formation or a protostellar phase, but immediately start with the ZAMS evolution of the formed massive stars. Then, in each time step, the age and initial mass of each star are used to determine the appropriate mass-loss rate and terminal velocity of the stellar wind.

While the mass-loss rates can be directly taken from the tracks by Ekström et al. (2012, for the corresponding scaling relations, see their section 2.6), we estimate terminal velocities ($v_{wind}$), which are not given in the tracks, according to their evolutionary status (defined from the surface abundances of the models, see Georgy et al. 2012).

(i) For OB-type stars and A supergiants, we use a slightly modified version of the scaling relations provided by Kudritzki & Puls (2000) and Markova & Puls (2008), namely $v_{wind} = 2.45\ v_{esc}$ for $T_{eff} > 2.3 \times 10^4$ K, $v_{wind} = 1.3\ v_{esc}$ for $T_{eff} < 1.8 \times 10^4$ K, and a linear interpolation in between (the so-called bistability jump, see Puls, Vink & Najarro 2008 and references therein). Here, $v_{esc}$ is the photospheric escape velocity corrected for the radiative acceleration by electron-scattering and $T_{eff}$ corresponds to the *corrected*, effective temperature as provided by the tracks.

(ii) For WR stars, we adapt observational data compiled by Crowther (2007), using linear interpolations. In particular, for WNL and WNE stars, we use $v_{wind} = 700$ km s$^{-1}$ for $T_{eff} < 2 \times 10^4$ K, and a linear inter/extrapolation between 700 and 2100 km s$^{-1}$ for $2 \times 10^4 < T_{eff} < 5 \times 10^4$ K, whilst for WC stars we use again $v_{wind} = 700$ km s$^{-1}$ for $T_{eff} < 2 \times 10^4$ K, and a linear inter/extrapolation between 700 and 2800 km s$^{-1}$ for $2 \times 10^4$ K $< T_{eff} < 8 \times 10^4$ K.

(iii) For red supergiants, we follow van Loon (2006), with $v_{wind} \propto L^{0.25}$, normalized to $v_{wind} = 10$ km s$^{-1}$at a luminosity of $L = 3 \times 10^4$ L$_\odot$.

(iv) Finally, the terminal velocities for objects in between blue and red supergiants (rather insecure) have been approximated by the geometric mean of the $v_{wind}$-values for the 'neighbouring' blue and red supergiants, resulting in typical values of $v_{wind} \approx 50$ km s$^{-1}$ for yellow supergiants.

Fig. 1 shows the stellar evolution tracks used in this work for four representative stars with initial masses of 9, 12, 20, and 85 M$_\odot$. The most massive stars show significantly higher mass-loss rates, wind terminal velocities, and wind luminosities, but about an order of magnitude shorter lifetimes (only ∼4 Myr for a star with 85 M$_\odot$). The bottom panel of Fig. 1 shows the cumulative wind energies, which depend strongly on the initial mass of the star. Stars with relatively low masses (∼9–20 M$_\odot$) release only little wind energy, i.e. $\sim 10^{-2}$–$10^{-4} \times E_{SN}$, where the typical energy released by a single SN event is $E_{SN} = 10^{51}$ erg. However, the most massive stars inject as much or even more energy in winds than in their final SN explosion. Following these tracks, it requires ∼ 6600 stars with 9 M$_\odot$ each to produce the same wind energy as a single 85 M$_\odot$ star.

For single stellar populations, stars at the lower end of our considered mass range (i.e. B-type stars) are considerably more numerous and have longer lifetimes than the WR- and massive O-stars that produce the strongest stellar winds.[1] Therefore, stellar winds only dominate the energy budget during the early evolution of the stellar population (for the first ≈5–20 Myr).

Stellar wind feedback: we apply the following prescription to model the wind energy input in our simulations.

[1] Energetically, i.e. with respect to luminosities and winds, WR-stars dominate (e.g. Leitherer, Robert & Drissen 1992; Doran et al. 2013).

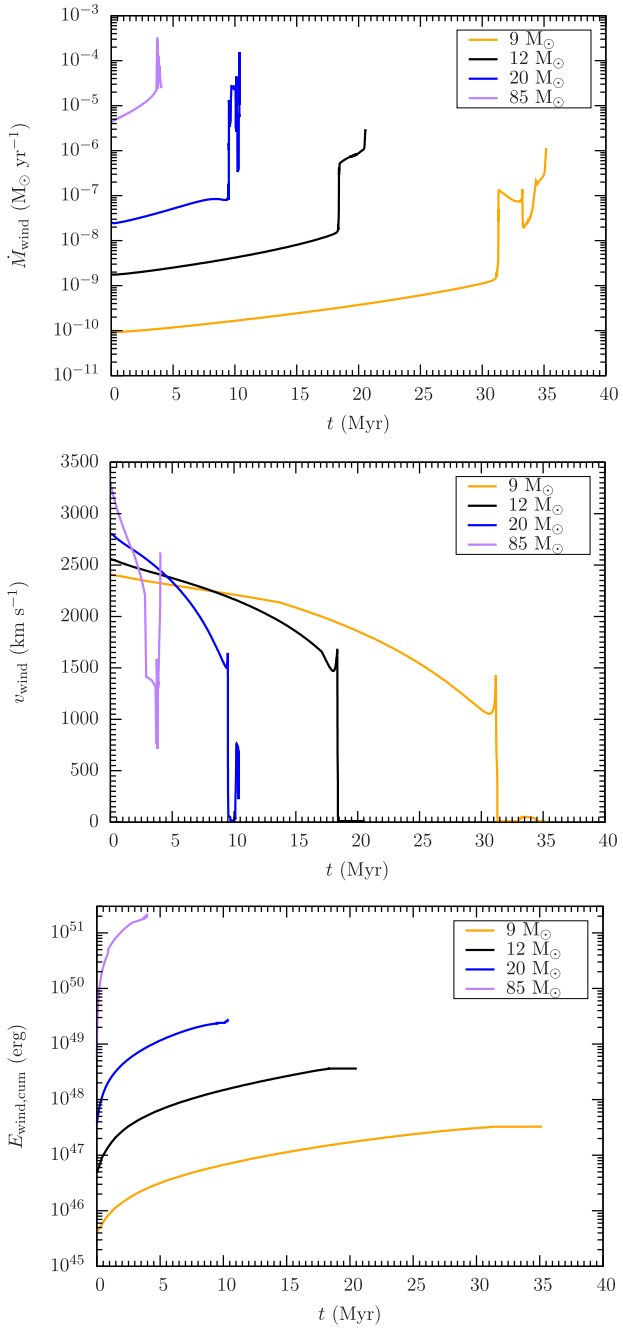


**Figure 1.** Mass-loss rates (top panel), wind terminal velocities (middle panel) and cumulative energies (bottom panel) for the stellar winds of four different massive stars with initial masses of 9 (orange), 12 (black), 20 (blue) and 85 (purple) $M_\odot$.

(i) For each cluster sink and at each time step, we calculate the total mechanical luminosity by adding up the contributions of all $N_\star$ stellar winds:

$$L_{\rm tot} = \frac{1}{2}\sum_{i=1}^{N_\star} \dot{M}_{\rm wind,i} \times v_{\rm wind,i}^2 \ [\rm erg\ s^{-1}]. \quad (5)$$

(ii) The total mass lost by all winds in the cluster is

$$\dot{M}_{\rm tot} = \sum_{i=1}^{N_\star} \dot{M}_{\rm wind,i}. \quad (6)$$

Within each time step $\Delta t$, we add a total mass of $\dot{M}_{\rm tot} \times \Delta t$ to the injection region, which we set equal to $r_{\rm accr}$. Per unit volume, the mass is evenly distributed amongst all the cells that overlap with the spherical injection region. Note that the mass of the cluster sink is reduced accordingly (the net sink mass can still increase due to the accretion of fresh gas).

(iii) The mass that is added to the injection region carries a certain amount of internal energy, which we take into account.

(iv) We inject the wind feedback in the form of kinetic energy, $e_{\rm inj}$, that we evenly distribute within $r_{\rm accr}$. Thus, we have

$$\begin{aligned} e_{\rm inj} &= \dot{e}_{\rm inj} \times \Delta t \\ &= L_{\rm tot} \times \Delta t \\ &= \frac{1}{2} M_{\rm inj} v_{\rm r}^2, \end{aligned}$$

where $M_{\rm inj} = M_{\rm inj,old} + \dot{M}_{\rm tot} \times \Delta t$ is the sum of the previously present gas mass within the injection region and the returned stellar wind material, and $v_{\rm r}$ is the radial velocity. The wind is assumed to be spherically symmetric and we neglect possible cancellation effects within the cluster sink due to wind collisions. The radial velocity applied within the injection region is hence computed from

$$v_{\rm r}^2 = 2\frac{L_{\rm tot} \times \Delta t}{M_{\rm inj}}. \quad (7)$$

SN feedback: once a star has reached the end of its lifetime, it is assumed to explode as a Type II SN. In our model, each SN releases an energy of $E_{\rm SN}$, which is typically injected in the form of thermal energy provided that the adiabatic phase of the SN remnant is resolved. If the density in the injection region is high, such that the Sedov–Taylor phase would be unresolved, we switch to a momentum input scheme (see Gatto et al. 2015, for a detailed description of the SN model). The mass of the SN progenitor star is also added to the injection region. For simplicity, we do not account for stellar remnants, which are unresolved. In the run FSN-n1e2 where stellar winds are not included, we still follow the evolution of each star to model the SN delay time.

Each feedback event is centred on the position of the cluster sink. We do not account for runaway stars that are ejected from their parental star clusters (see e.g. Li et al. 2015, for a discussion). Moreover, we neglect the slow winds from stars with $M \leq 8\,M_\odot$. Type Ia SNe originating from an old stellar population are also not included in our model.

## 2.5 Simulation set-up

### 2.5.1 *List of simulations*

We present a set of six simulations (see Table 1), with which we are able to show the effect of the different feedback mechanisms. For reference, we include run NoF-n1e2, which is a run with clustered star formation but without feedback. Then we switch on either wind feedback (run FW-n1e2) or SN feedback (run FSN-n1e2), or both (run FWSN-n1e2). As a second parameter, we increase the sink density threshold from $\rho_{\rm sink} = 2 \times 10^{-22}\,\rm g\,cm^{-3}$ (all runs with ending -n1e2) to $\rho_{\rm sink} = 2 \times 10^{-21}\,\rm g\,cm^{-3}$ (run FWSN-n1e3) and $\rho_{\rm sink} = 2 \times 10^{-20}\,\rm g\,cm^{-3}$ (run FWSN-n1e4), respectively.

**Table 1.** Overview of all presented simulations. We list the run names (column 1), the sink density threshold $\rho_{\rm sink}$ (column 2), and the included feedback mechanisms (stellar winds in column 3, SNe in column 4).

| Name | $\rho_{\rm sink}$ $[2 \times 10^{-24}\,{\rm g\,cm^{-3}}]$ | Wind | SN |
|---|---|---|---|
| NoF-n1e2 | $10^2$ | No | No |
| FSN-n1e2 | $10^2$ | No | Yes |
| FW-n1e2 | $10^2$ | Yes | No |
| FWSN-n1e2 | $10^2$ | Yes | Yes |
| FWSN-n1e3 | $10^3$ | Yes | Yes |
| FWSN-n1e4 | $10^4$ | Yes | Yes |

#### 2.5.2 *Initial conditions*

The initial gas density profile (see Paper I and Paper II) is uniform in $x$- and $y$-direction but follows a Gaussian distribution in the $z$-direction

$$\rho(z) = \rho_0 \exp\left[-\frac{1}{2}\left(\frac{z}{z_0}\right)^2\right], \quad (8)$$

with a scaleheight of $z_0 = 30\,{\rm pc}$ and a mid-plane density of $\rho_0 = 9 \times 10^{-24}$ g cm$^{-3}$. At large heights above the mid-plane, we truncate the Gaussian distribution at the background density of $\rho_{\rm bg} = 10^{-28}\,{\rm g\,cm^{-3}}$. Altogether, the initial gas surface density of the disc is $\Sigma_{\rm gas} = 10\,{\rm M_\odot\,pc^{-2}}$ and the total mass in the computational domain is $M_0 = 2.55 \times 10^6\,{\rm M_\odot}$.

We set the initial temperature within the disc mid-plane to $T = 4500$ K and assume vertical pressure equilibrium to compute the temperature profile. Therefore, the halo gas is hot with a temperature of $T = 4 \times 10^8$ K. According to the initial temperature profile, all hydrogen is initially atomic near the disc mid-plane and partially or fully ionized at larger scaleheights. Carbon is fully ionized everywhere in the computational domain.

To create inhomogeneities in the gas distribution and to partially support the disc against gravitational collapse, we initially drive turbulent motions in the disc. This is necessary as otherwise all gas would collapse towards the mid-plane and cause a strong burst of star formation. On the largest possible modes in the disc plane, $k = 1$ and 2 corresponding to the box size of 500 pc and half of the box size, the turbulent energy is injected with a flat power spectrum and a thermal mix of solenoidal (divergence-free) to compressive (curl-free) modes of 2:1. The energy input is adjusted such that the global, mass-weighted, 3D root-mean-square (rms) velocity remains constant at $v_{\rm 3D,\,rms} \sim 10\,{\rm km\,s^{-1}}$. The turbulent energy input is evolved with an Ornstein–Uhlenbeck random process (Eswaran & Pope 1988) with a phase turnover time, which corresponds to the turbulent crossing time in the $x$ and $y$ directions of $\sim$50 Myr. The turbulence driving is switched off once the first sink particle has formed, which happens after $\gtrsim$9 Myr ($t_{\rm sink,\,0} = 9$ Myr for the simulations with the lowest sink density threshold).

## 3 QUALITATIVE DISCUSSION OF THE SIMULATIONS

In Fig. 2, we give one example for the resulting temperature, density, and chemical structure of the ISM[2] for run FWSN-n1e3 at $t = 45$ Myr. From left to right, we show a slice of the gas density at $y = 0$ (top) and $z = 0$ (bottom) and temperature followed by the column densities of all gas and the different species that we trace in the simulation, i.e. $H^+$, H, $H_2$, and CO, respectively. The filled, white circles show the position of the formed cluster-sink particles. In this simulation, the SFR is low and there are not many clusters. Similar figures for all simulations at comparable times ($t \approx t_{\rm sink,\,0} + 31$ Myr) after the formation of the first cluster at $t_{\rm sink,\,0}$ are shown in Appendix A. The formation time of the first cluster in each simulation is listed in Table 2.

Run FWSN-n1e4 features significant amounts of $H_2$ and CO, which are organized in filamentary and clumpy structures near the disc mid-plane. The cluster-sink particles form within the densest clumps and redistribute the surrounding gas by wind and SN feedback. In particular, stellar winds disperse the gas early during cluster formation and evolution. SNe heat the gas efficiently but their onset is delayed with respect to cluster formation.

For comparison, we show the time evolution of the total gas column density for all six simulations (see Table 1) in Figs 3–5. At first, we show the run without feedback for reference (Fig. 3, left-hand panel). The lack of pressure support from stellar feedback results in a compact configuration around the disc mid-plane. In the right-hand panel, we depict the evolution of run FW-n1e2 with feedback from stellar winds, which are emitted by the massive stars within the forming stellar clusters. The cluster sinks are allowed to accrete throughout the simulation and a new massive star is formed every time a mass of $120\,{\rm M_\odot}$ has been accreted on to the cluster (see Section 2.4). We randomly assign a mass to each formed star (sampled from the high-mass stellar IMF), so most of the forming stars are B-type stars and contribute only weak wind feedback which does not heat the gas efficiently.

The disc scaleheight increases dramatically when SN feedback is included (Fig. 4). Here, we note that the ISM in the run with only SN feedback (left-hand panel) appears to be more clumpy and structured than run FWSN-n1e2 with wind and SN feedback (right-hand panel). Early feedback by stellar winds suppresses gas accretion on to young cluster sinks. Gas that is unbound by stellar wind feedback is available within the ISM, causing the ISM to be somewhat more diffuse. In particular, the outflowing gas is slightly colder in this simulation.

Fig. 5 illustrates the impact of the sink density formation threshold, $\rho_{\rm sink}$. For higher $\rho_{\rm sink}$, the number of cluster sinks and hence the SFR is significantly reduced. Therefore. we have less feedback, which results in a smaller disc scaleheight and less-to-no outflowing gas. In the following sections, we discuss these findings quantitatively.

## 4 HOW FEEDBACK REGULATES STAR-CLUSTER FORMATION

The presented set of simulations allows us to determine the relative importance of stellar wind and SN feedback in terms of regulating the SFR in the simulated portions of the galactic disc.

### 4.1 Mass evolution and star formation rates

There are different ways to measure the SFR surface density in our simulations. Naively, one could just count how much gas is collapsing into sink particles (representing the stellar population)

[2] Movies of all simulations are available at http://www.astro.uni-koeln.de/silcc.

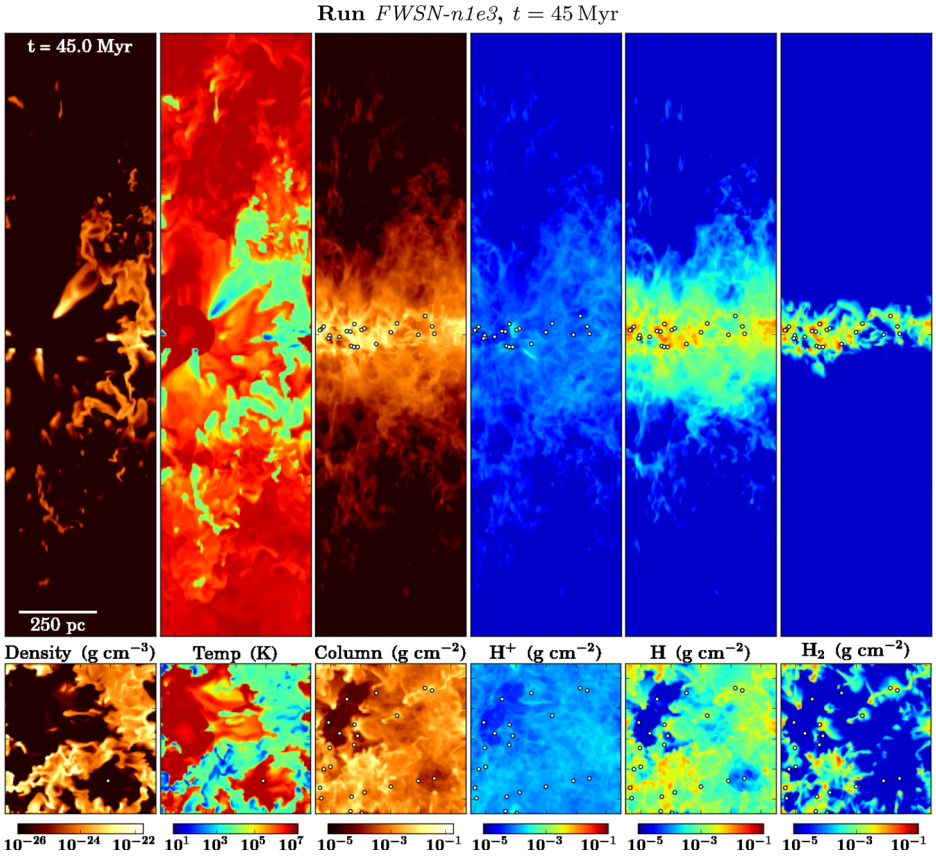


**Figure 2.** Run FWSN-n1e3 with stellar wind and SN feedback from cluster sinks that are introduced above $\rho_{\rm sink} = 2 \times 10^{-21}\,{\rm g\,cm^{-3}}$ at $t = 45$ Myr as seen edge-on (upper panels) and face-on (lower panels). From left to right: density slice, temperature slice, column density, and the column densities of $H^+$, H, and $H_2$, respectively. The filled circles show the location of the cluster-sink particles.

**Table 2.** For each simulation (column 1) we list the time at which the first star cluster forms (column 2), the time at which we stop the simulation (column 3), and the total number of massive stars formed (column 4; see Fig. 9). In column 5, we list the average SN rate per Myr, where we average over $t_{\rm stop} - t_{\rm sink,\,0}$. In columns 6 and 7, we give the maximum and the median of the cluster-sink mass distribution (see Fig. 10), and in column 8 we list the logarithmic mean accretion time of all clusters in the respective simulations.

| Run name | $t_{\rm sink,\,0}$ (Myr) | $t_{\rm stop}$ (Myr) | $N_{\star,\rm tot}$ | $\dot{N}_{\rm SN}$ (Myr$^{-1}$) | $M_{\rm sink,max}$ (M$_\odot$) | $M_{\rm sink,med}$ (M$_\odot$) | $< t_{\rm sink,max} >_{\rm log}$ (Myr) |
|---|---|---|---|---|---|---|---|
| NoF-n1e2 | 9.06 | 80.0 | 14 082 | – | $5.1 \times 10^5$ | $9.8 \times 10^3$ | 27.9 |
| FW-n1e2 | 9.06 | 80.0 | 3705 | – | $4.4 \times 10^4$ | $2.0 \times 10^3$ | 0.12 |
| FSN-n1e2 | 9.06 | 80.0 | 5350 | 70.2 | $7.2 \times 10^4$ | $1.2 \times 10^4$ | 4.51 |
| FWSN-n1e2 | 9.06 | 80.0 | 2710 | 36.9 | $3.7 \times 10^4$ | $5.6 \times 10^3$ | 0.01 |
| FWSN-n1e3 | 13.9 | 85.0 | 1656 | 17.2 | $3.9 \times 10^4$ | $8.5 \times 10^2$ | 0.69 |
| FWSN-n1e4 | 30.3 | 101.0 | 358 | 4.5 | $1.8 \times 10^4$ | $2.5 \times 10^3$ | 0.26 |

within a given time bin $\Delta t$. We call this the *instantaneous SFR*, $\Sigma_{\rm SFR_{inst}}$, which is computed as

$$\Sigma_{\rm SFR_{inst}}(t) = \frac{1}{A} \sum_{j=1}^{N_{\rm sink}} \dot{M}_{{\rm sink},\,j}(\Delta t) \;\; [{\rm M_\odot\ yr^{-1}\ kpc^{-2}}], \tag{9}$$

for $t - \frac{\Delta t}{2} < t < t + \frac{\Delta t}{2}$ and the area of the computational domain in the disc mid-plane $A = (0.5\,{\rm kpc})^2$.

However, the SFR derived in this way depends on $\Delta t$ and is not directly comparable to the SFR an observer would measure, e.g., when tracing the SFR with H$\alpha$ emission. The H$\alpha$ emission sensitively depends on the presence of OB and WR stars, which have short lifetimes of ∼5–40 Myr. Since we follow every massive star, $i$, in our simulation (one massive star is formed for each 120 M$_\odot$ of gas that is turned into stars), we can use the current number of massive stars and their respective lifetime, $t_{{\rm OB},\,i}$, to estimate an *observable SFR surface density*, $\Sigma_{\rm SFR_{OB}}$, as

$$\Sigma_{\rm SFR_{OB}}(t) = \frac{1}{A} \sum_{i=1}^{N_*} \frac{120\,{\rm M_\odot}}{t_{{\rm OB},i}}\,, \tag{10}$$

for $t_{{\rm form},\,i} < t < t_{{\rm form},\,i} + t_{{\rm OB},\,i}$, where $t_{{\rm form},\,i}$ is the formation time of massive star $i$ and $N_\star$ is the number of 'active' massive stars at time $t$.

In Fig. 6, we show $\Sigma_{\rm SFR_{inst}}$ for $\Delta t = 1$ Myr (grey bars) and $\Sigma_{\rm SFR_{OB}}$ (red lines), as well as the average $\Sigma_{\rm SFR_{OB}}$ (red dotted line) for the

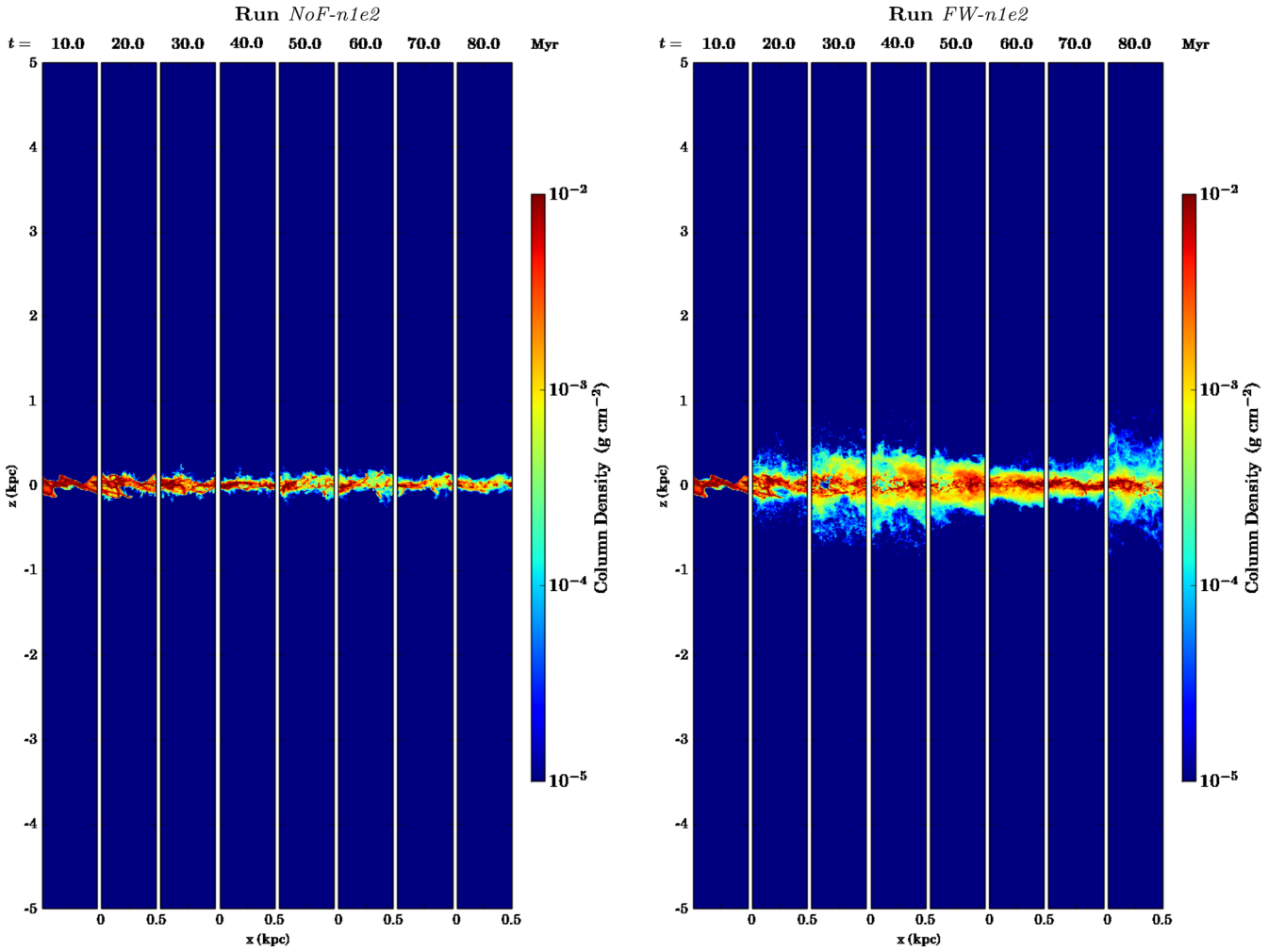


**Figure 3.** Time evolution (from left to right) of the total gas column density. Left: simulation NoF-n1e2 without feedback. In this case, no outflows are driven and the gas collapses to the mid-plane. Right: simulation FW-n1e2 with stellar winds (no SNe) originating from the massive stars within the cluster-sink particles.

different simulations (different panels). A bin size of $\Delta t = 1$ Myr corresponds to ∼1000 time steps in the simulations with feedback (the typical time step is $\sim 10^3$ yr). Young star clusters (with ages $\lesssim$5–10 Myr, i.e. before the first SN explodes) have high accretion rates and contribute most to $\Sigma_{\rm SFR_{inst}}$. We find that $\Sigma_{\rm SFR_{inst}}$ becomes more bursty in the presence of stellar winds (e.g. NoF-n1e2 versus FW-n1e2) that truncate cluster growth, as well as for a lower total amount of star formation per unit area, $\Sigma_{\rm SF,tot} = \int_0^{t_{\rm stop}} \Sigma_{\rm SFR_{inst}} {\rm d}t$. Overall the O- and B-type star lifetimes are still long enough to hide the time variation from an observer, who would measure $\Sigma_{\rm SFR_{OB}}$. The variation is significant and thus $\Sigma_{\rm SFR_{OB}}$ can be orders above the current SFR as well as up to a factor of 10 below it.

In Fig. 7 (left-hand panel), we show the total mass in cluster-sink particles as a function of time for all six simulations. In run NoF-n1e2, most of the gas (∼80 per cent) has collapsed into sinks by $t = 80$ Myr, followed by run FSN-n1e2 with ∼20 per cent in sinks. Until the very end of the simulation, runs FW-n1e2 and FWSN-n1e2 evolve similarly and ∼10 per cent of the gas is converted into sinks. This shows that stellar wind feedback efficiently regulates star formation right after the first massive star was born. SN feedback acts with a time delay and therefore allows for more star formation. Wind and SN feedback together closely follow the case of only wind feedback because the gas that would be available to accrete on to formed sinks is already unbound by the stellar winds and SNe have little additional effect. We note that this result might not be generally applicable with increasing gas surface density in the disc. When the sink density threshold is increased, the mass in sinks decreases to ∼1 per cent for FWSN-n1e4. In addition, star formation starts later in these simulations and we have therefore run them for longer (see $t_{\rm sink,\,0}$ as listed in Table 2).

The later onset of star formation in simulations with higher $n_{\rm sink}$ can be compared with the free-fall time at the given $n_{\rm sink}$, $\tau_{\rm ff} = (3\pi/(32\,G m_{\rm p} n_{\rm sink}))^{1/2}$. For example, we have $\tau_{\rm ff}(n_{\rm sink} = 10^2\,{\rm cm}^{-3}) \approx 5$ Myr, while we assume that star formation proceeds instantaneously within the cluster sinks formed at this density. In 5 Myr, the gas has quite some time to move around (a typical turbulent velocity of 10 km s$^{-1}$ roughly corresponds to 10 pc Myr$^{-1}$ and hence a distance of 50 pc can easily be crossed) and may not be accreted on to a cluster sink, which is introduced at a higher $n_{\rm sink}$. In addition, fewer cells are filled with higher density gas in a turbulent environment (consider a lognormal structure of the volume-weighted density

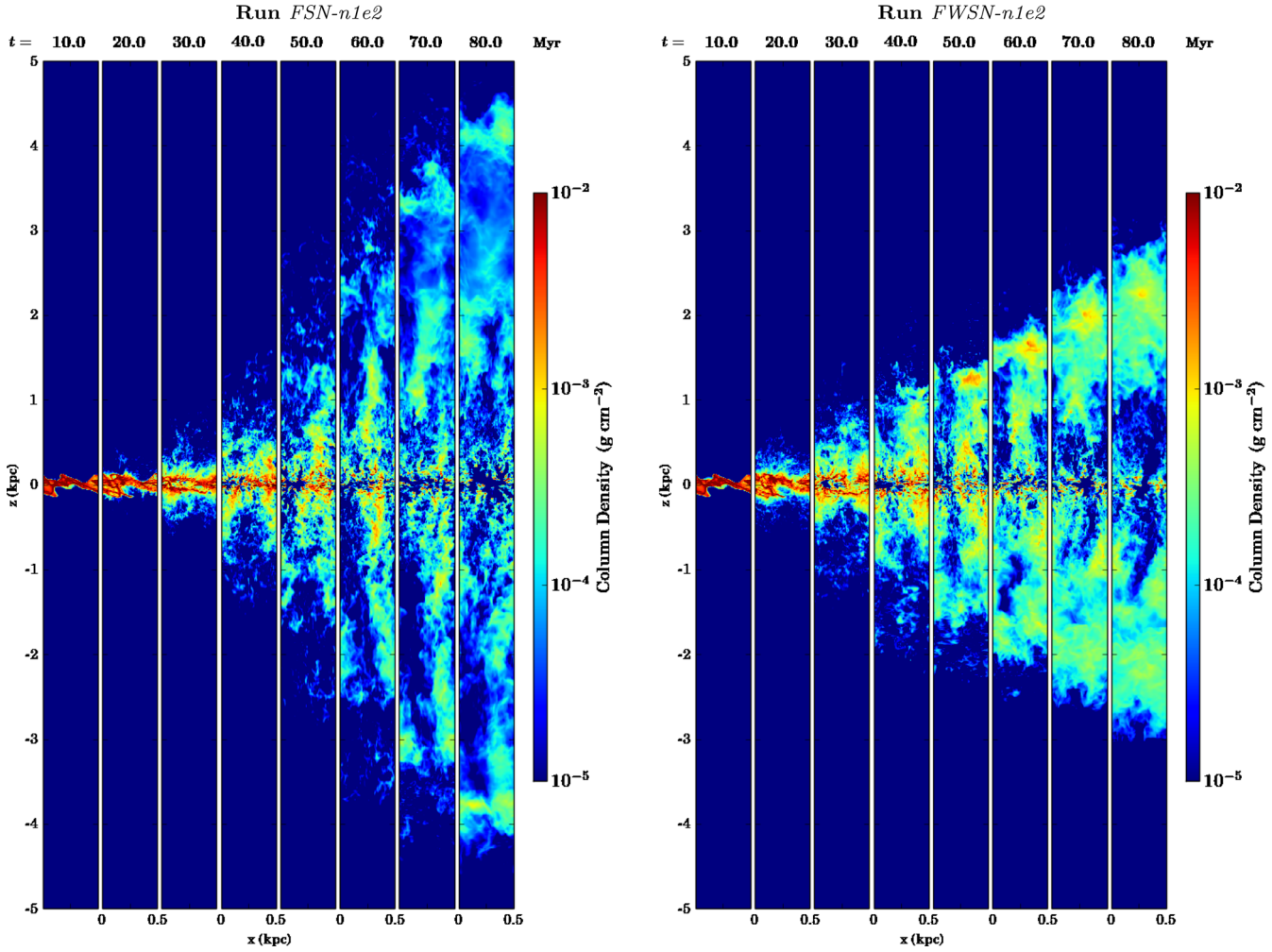


**Figure 4.** Same as Fig. 3 for simulation FSN-n1e2 with just SN explosions (left-hand panel). This simulation has a high SFR and drives the strongest outflows. Right: simulation FWSN-n1e2 with both, stellar winds and SN explosions. Here, stellar winds reduce the SFR and outflow.

Probability distribution function) and therefore the sink formation becomes more stochastic as fewer cells meet the density formation criterion for higher $n_{\rm sink}$. Formally, the high-density thresholds are unresolved with respect to e.g. the Truelove criterion (see Section 2.3).

In Fig. 7 (right-hand panel), we show $\Sigma_{\rm SFR_{OB}}$ as a function of time for all simulations. The horizontal, grey, dashed line shows the SFR surface density corresponding to the KS value at $\Sigma_{\rm gas} = 10\,{\rm M_\odot\,pc^{-2}}$ and the light-grey band indicates an uncertainty of a factor of 2. Clearly, runs without feedback or with SN feedback alone have too high $\Sigma_{\rm SFR_{OB}}$, while the value found for run FWSN-n1e4 is a bit low. We note that runs with higher threshold densities (FWSN-n1e3 and FWSN-n1e4) have relatively flat SFRs and are missing the initial peak.

We place our simulation results on the familiar KS diagram (Kennicutt 1998) in Fig. 8. Here, we plot the derived average surface mass density in atomic plus molecular hydrogen, $\Sigma_{\rm H+H_2}$, against the average $\Sigma_{\rm SFR_{OB}}$, where the averages were computed between $t_{\rm sink,\,0}$ and $t_{\rm stop}$. We also show the observations of 23 (11 dwarfs and 12 large spirals) nearby *normal* star-forming galaxies by Leroy et al. (2008, yellow points). These are composed of hundreds of radial profiles of $\Sigma_{\rm SFR}$, $\Sigma_{\rm H}$, and $\Sigma_{\rm H_2}$ (only for spirals) at 800 pc (spirals) and 400 pc (dwarf) resolution. We multiply their SFRs by a factor of 1.59 in order to rescale them from a Kroupa (2001) to a Salpeter (1955) IMF. The thin, blue line again indicates the standard KS relation (as in Fig. 7; Kennicutt 1998):

$$\frac{\Sigma_{\rm SFR_{KS}}}{\rm M_\odot\,yr^{-1}\,kpc^{-2}} = 2.5\times10^{-4}\left(\frac{\Sigma_{\rm H+H_2}}{\rm M_\odot\,pc^{-2}}\right)^{1.4}. \quad (11)$$

Simulations without stellar wind feedback result in a $\Sigma_{\rm SFR}$ that is too high and do not agree well with observations.

In Fig. B1 (Appendix B), we show the corresponding time evolution of the total gas mass (top-left panel), and of the mass fractions of atomic hydrogen (top right), ionized hydrogen (bottom left), and molecular hydrogen (bottom right), all normalized to the total gas mass at $t = 0$, $M_0$ (see Section 2.5.2). The total gas mass evolution is complementary to the sink mass evolution.

### 4.2 Regulation of star formation by stellar winds

Depending on the simulation, our cluster-sink sub-grid model results in a population of a few $10^2$–$10^3$ massive stars (see Fig. 9, top-left panel). Simulations with higher overall SFRs also form more massive stars. With a few thousand massive stars, we achieve a good random sampling of the IMF for massive stars with $M_* \lesssim 80\,{\rm M_\odot}$.

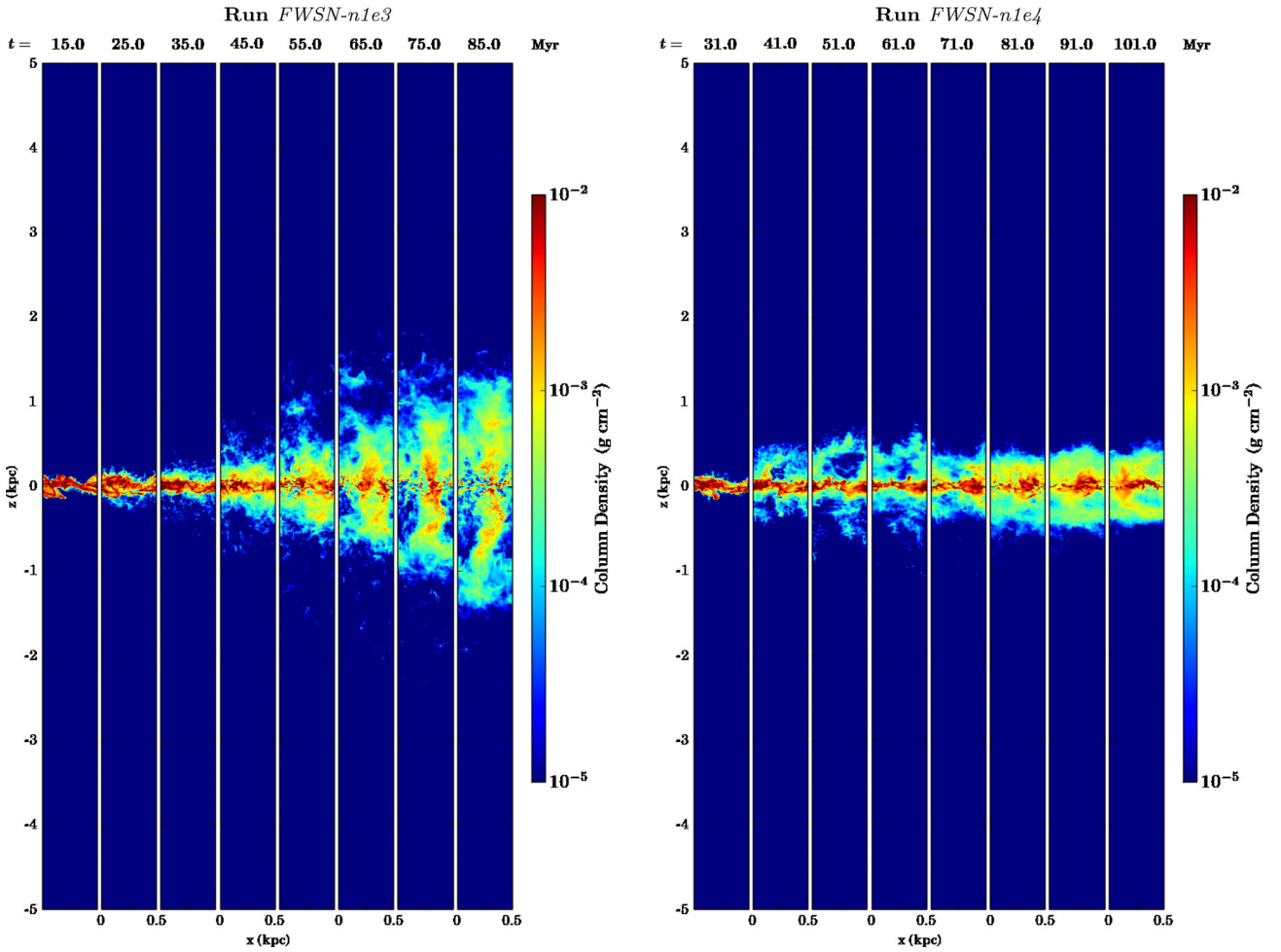


**Figure 5.** Same as Fig. 3 for simulations FWSN-n1e3 (left-hand panel) and FWSN-n1e4 (right-hand panel), both with stellar winds and SNe. In these simulations, the formation of cluster-sink particles is enabled above $\rho_{\rm sink} = 2 \times 10^{-21}\,{\rm g\,cm^{-3}}$ and $2 \times 10^{-20}\,{\rm g\,cm^{-3}}$, respectively. The SFR decreases with increasing $\rho_{\rm sink}$ leading to smaller disc scaleheights.

Therefore, the different simulations give the same slope of the IMF but a different $y$-axis offset (see top-right panel of Fig. 9, where we plot the massive star IMF using a bin size of $5\,{\rm M}_\odot$). Since the slope of the IMF is very steep, we only form a small number of very massive stars ($\lesssim$10 stars per bin at $\sim$100 $\rm M_\odot$). Due to the low number statistics in the highest mass bins, all simulations with $n_{\rm sink} = 10^2\,{\rm cm^{-3}}$ have comparable numbers of very massive stars. Runs with higher $n_{\rm sink} = 10^3$–$10^4\,{\rm cm^{-3}}$ form fewer stars and consequently have fewer very-high-mass stars.

In the lower panels of Fig. 9, we show the cumulative energy input from stellar winds (left-hand panel) and from SNe (right-hand panel). In runs with winds and SNe, the SN energy input is only a factor of $\sim$2.5–3 larger than the cumulative wind energy input. Note that this applies for the solar metallicity case and that the ratio might be different in lower metallicity environments as lower metallicity stars have, during most of their evolution, winds with lower mass-loss rates (e.g. Kudritzki, Pauldrach & Puls 1987; Vink, de Koter & Lamers 2001; Krtička 2006; Mokiem et al. 2007; Gräfener & Hamann 2008) and somewhat lower terminal velocities (Leitherer et al. 1992; Krtička 2006). Although the very massive stars are so rare and only live for a very short time, they are the ones that contribute the most wind energy (see cumulative wind energy input shown in Fig. 1). This renders the wind energy input to be quite stochastic for individual star-cluster-forming regions, depending on the masses of the individual very massive stars.

To quantitatively assess the differential impact of stellar winds and SNe on star cluster formation, we investigate the accretion history of the forming cluster-sink particles in Fig. 10. In the left-hand panel, we show the cumulative mass distribution of all cluster sinks at the time of formation (thin dotted lines) and at their maximum mass (solid lines). We define the *cluster formation time*, $t_{\rm sink,\,max}$, as the time it takes each cluster sink to reach its maximum mass. The cumulative distribution of maximum cluster masses is shifted to higher masses for all simulations, which indicates that a significant amount of mass is gained by gas accretion. This subsequent gas accretion tends to steepen the cumulative mass distributions [in the left-hand panel of Fig. 10, the cumulative distributions of the maximum masses (solid lines) are steeper than the corresponding cumulative distributions of the initial masses shown by dotted lines), which means that the variance of the actual mass distributions, which have an approximately lognormal shape (the corresponding cumulative distributions can be represented with an error function), decreases with time.

For runs NoF-n1e2, FSN-n1e2, and FWSN-n1e2, the number of formed cluster sinks is comparable ($\sim$40) and also the initial cluster-sink mass distributions are very similar. However, the maximum mass distributions are different, since the runs with more feedback subsequently accrete less mass. Therefore, the run without feedback forms the most massive clusters with up to $M_{\rm sink,\,max} \sim 5 \times 10^5\,{\rm M}_\odot$ and a median mass of $M_{\rm sink,\,med} \sim 10^4\,{\rm M}_\odot$,

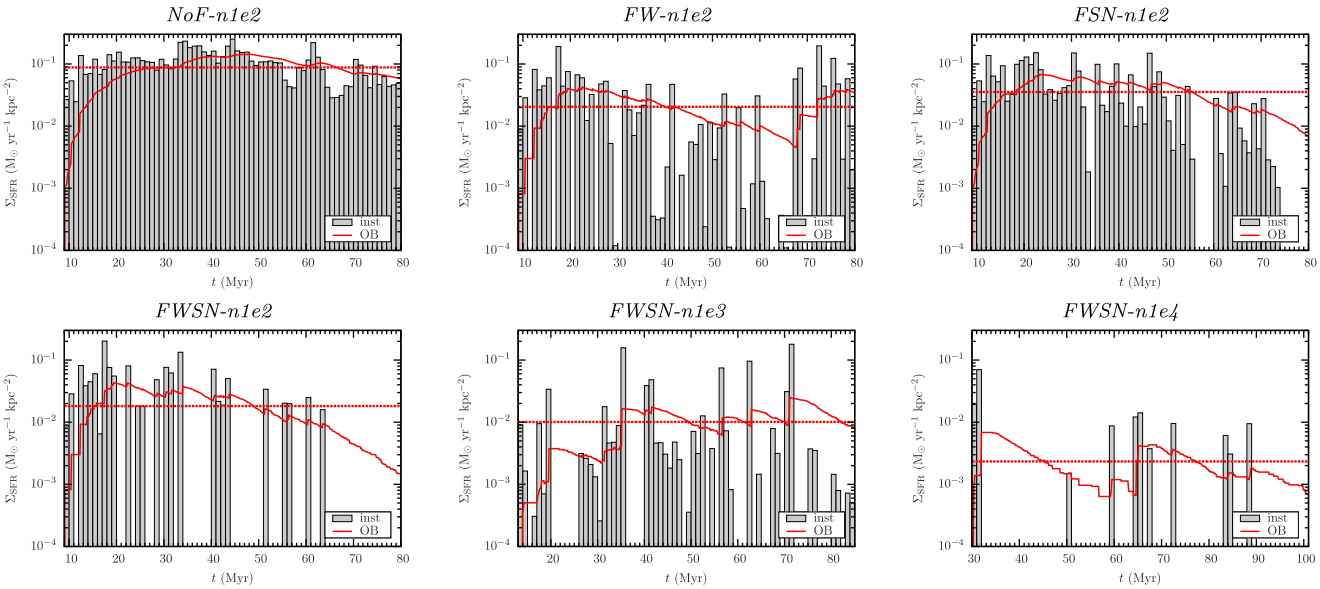


**Figure 6.** Evolution of the $\Sigma_{SFR}$ for all six simulations. The grey bins represent the instantaneous SFR surface densities, $\Sigma_{SFR_{inst}}$ (gas locked in sinks, see equation 9), while the red lines indicate the 'observed' values, $\Sigma_{SFR_{OB}}$ as derived from the O- and B-type star lifetimes (see equation 10). The horizontal, red dotted line is the average $\Sigma_{SFR_{OB}}$ over 71 Myr of star formation activity. In particular, the wind feedback (the FW simulations) renders star formation more stochastic by early termination of cluster-sink growth.

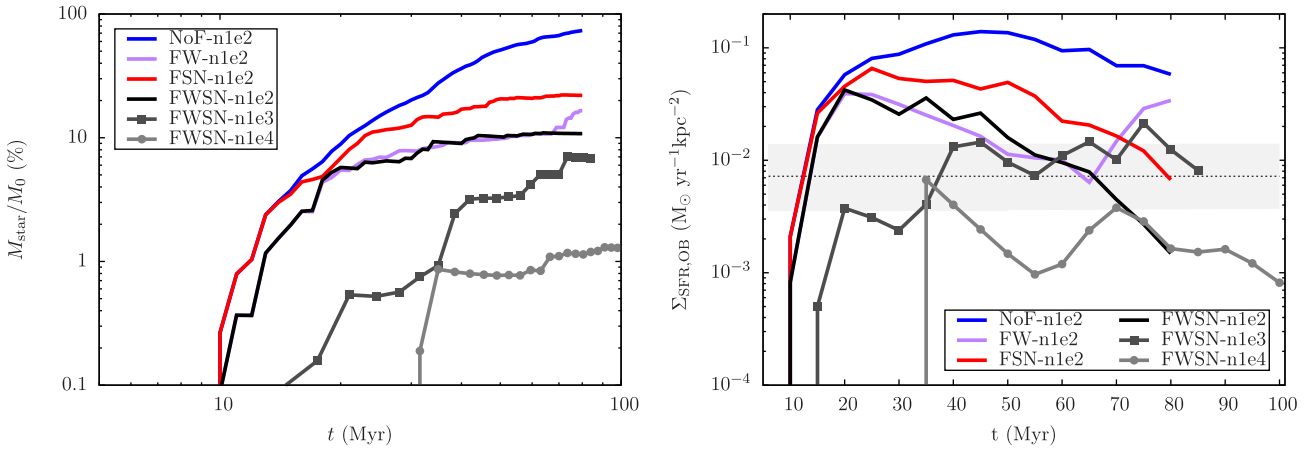


**Figure 7.** Left-hand panel: time evolution of the total mass in cluster-sink particles, i.e. in stars, for the six simulations. The no-feedback run (blue line) has the highest SFR and is shown for reference. Stellar winds suppress the accretion of gas on to the sinks immediately after the first massive stars form and efficiently limit sink formation (by at least a factor of 2, see purple line), while SN feedback is delayed and is therefore less efficient. Star formation is also reduced for higher sink density thresholds (grey lines). Right-hand panel: time evolution of the SFR surface density for the six simulations. The curves are slightly smoothed with respect to Fig. 6 to reduce noise. The grey dashed line indicates $\Sigma_{SFR}$ as expected from the KS relation for $\Sigma_{gas} = 10\,M_\odot\,pc^{-2}$ and the grey band indicates a factor of 2 uncertainty. Only runs with stellar wind feedback lie in the observed range with the best-fitting simulation being FWSN-n1e3. SN feedback alone is not efficient enough and acts too late to significantly limit the SFR (red line).

the run with only SN feedback forms somewhat lower mass clusters with up to $M_{sink,\,max} \sim 7 \times 10^4\,M_\odot$ and a median mass of $M_{sink,\,med} \sim 10^4\,M_\odot$, and the run with SN and stellar wind feedback forms even lower mass clusters with a maximum mass of up to $M_{sink,\,max} \sim 3.7 \times 10^4\,M_\odot$ and a median of $M_{sink,\,med} \sim 5.6 \times 10^3\,M_\odot$.

Interestingly, run FW-n1e2 with just winds forms approximately twice as many cluster sinks, where most of the additional clusters have low masses ($\lesssim 2 \times 10^3\,M_\odot$) and therefore do not contribute significantly to the total mass in cluster sinks. For higher sink density thresholds with wind and SN feedback, the SFR is lower and fewer clusters form in the case of run FWSN-n1e4. The maximum masses are comparable to run FWSN-n1e2 but the median masses are somewhat lower with ~0.85–2.5 $\times$ 10$^3$ M$_\odot$ (we list $M_{sink,\,max}$ and $M_{sink,\,med}$ for all clusters in Table 2). For comparison, in the Milky Way there are only a handful of known star clusters with masses above $2 \times 10^4\,M_\odot$ (see e.g. Piskunov et al. 2008; Fujii & Portegies Zwart 2016, and references therein) and therefore the run without stellar feedback is in clear disagreement with observations. The runs including stellar wind feedback show the best agreement

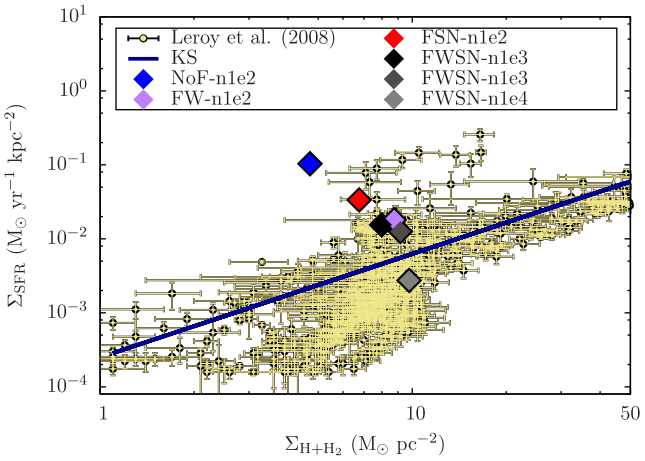


**Figure 8.** Mean SFR surface density versus mean total gas (H and $H_2$) surface density for the different simulations. The means were computed between 30 and 80 Myr. The simulations with wind feedback agree best with observations. The light-yellow points with black contours show the observational data from Leroy et al. (2008), while the dark-blue line represents the KS relation.

with the solar neighbourhood observations of young star clusters (Lada & Lada 2003), where the solar neighbourhood motivates our initial conditions.

We note that our result of an approximately lognormal cluster mass function is not in disagreement with the observationally established power-law mass distribution with a slope of −2 (de Grijs et al. 2003; Gieles et al. 2006). Due to small number of cluster that are formed in our volume, we can only sample the peak of the cluster mass function. A more detailed analysis of the slope of the cluster mass function is unfortunately not possible here and requires simulations of full galactic discs or at least significantly larger volumes.

In the right-hand panel of Fig. 10, we plot the cluster formation time $t_{\rm sink,\,max}$ as a function of maximum cluster mass. This is equivalent to the time-scale on which a cluster accretes gas efficiently. Clearly, runs without stellar wind feedback accrete for a long time, from 5 Myr up to 71 Myr, which is the maximum possible accretion time for run NoF-n1e2, $t_{\rm sink,\,max} = t_{\rm stop} - t_{\rm sink,\,0}$, where $t_{\rm stop} = 80$ Myr and $t_{\rm sink,\,0} \approx 9$ Myr for the first cluster-sink particle. For run FSN-n1e2 (red points), $t_{\rm sink,\,max} \sim 4.51$ typically corresponds to the lifetime of the most massive star that first explodes as a SN, i.e. the minimum SN delay time. Overall, these clusters all accrete for about the same but relatively long time-scale

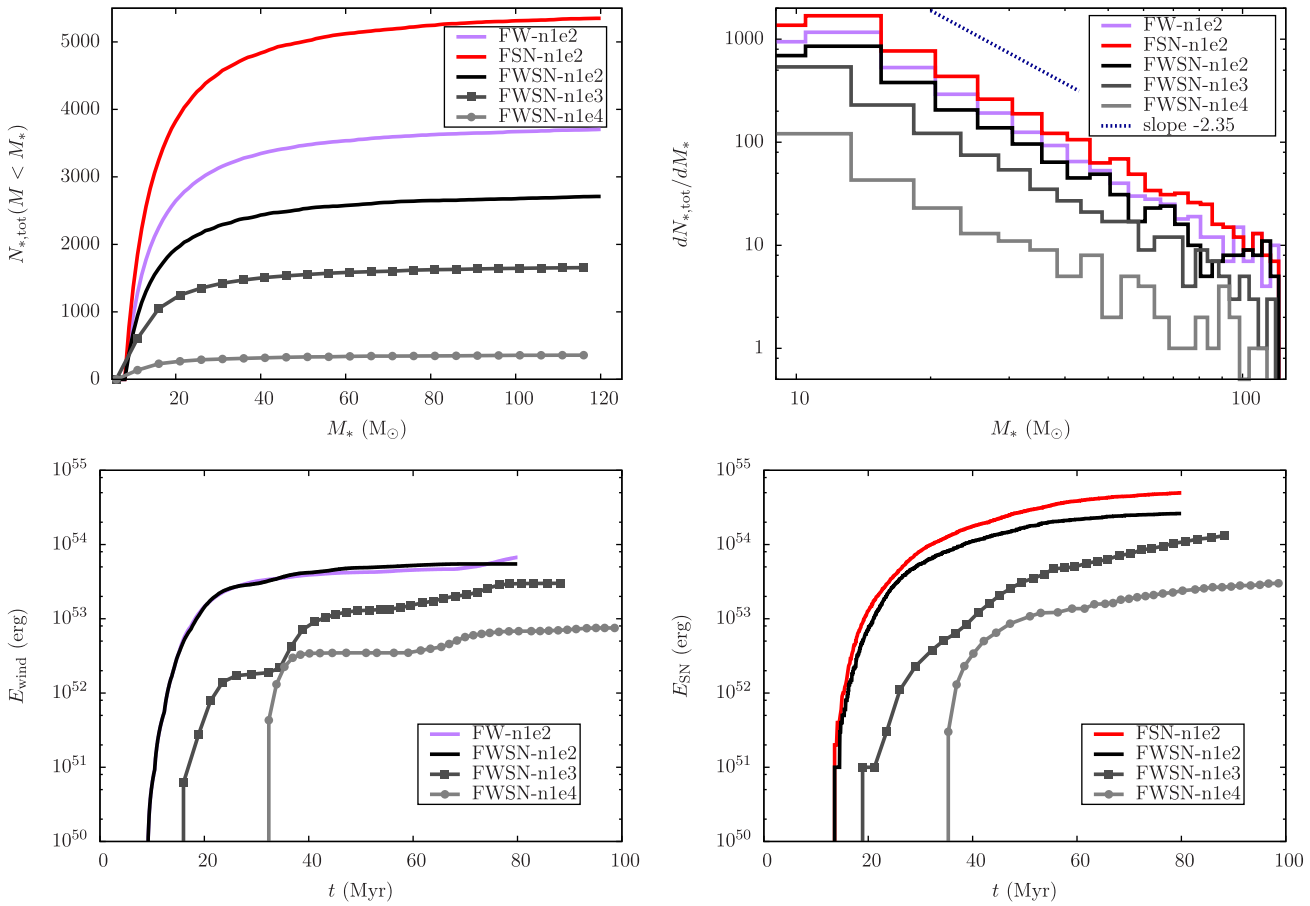


**Figure 9.** Top-left panel: cumulative distribution of all massive stars, $N_{\star,\,\rm tot}$, that form in the simulations with feedback. Simulations with a higher mass in cluster-sink particles also form a larger number of massive stars. Top-right panel: the stellar IMF of the massive stars formed in these runs for a mass bin size of 5 $M_\odot$. All show a Salpeter slope (as indicated by the dotted, dark-blue line) modulo some noise from the random sampling. Bottom panels: cumulative wind energy input (left) and SN energy input (right) from all massive stars in the simulations. The energy input from SN explosions is only a factor of ∼3 higher than from stellar winds.

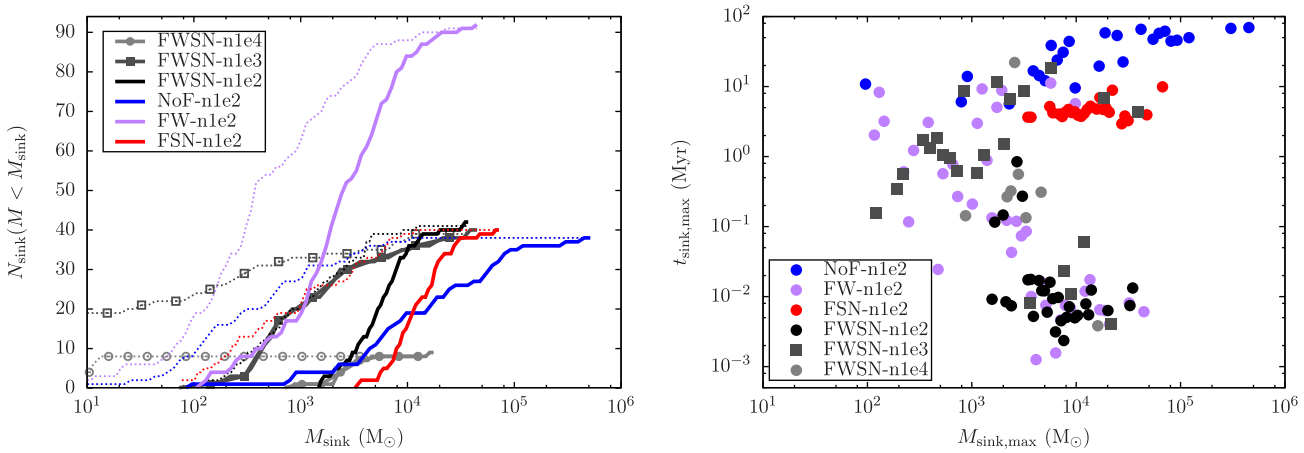


**Figure 10.** Left-hand panel: cumulative mass distribution for all cluster sinks in the simulations at the time of their formation (dotted lines) and at their maximum mass (solid lines). There is substantial gas accretion on to most of the cluster-sink particles, which causes the distributions (dotted versus solid at the same colour) to shift towards higher masses. At a given threshold density SNe (red line) reduce the cluster mass range but not their number (compare to the run without feedback, blue line). Wind feedback in addition reduces the cluster masses even more (black line). Wind feedback alone results in the formation of more clusters at lower masses (purple line). Right-hand panel: cluster growth time-scales – the time it takes each sink particle to reach its maximum mass, $t_{\rm sink,\,max}$, plotted against the respective maximum sink mass. Runs with wind feedback form a population of lower mass sinks with short accretion times, whereas runs without wind feedback (blue and red dots) accrete for longer and assemble higher maximum masses.

of ∼5 Myr and thus, all become quite massive. All clusters have masses above $\sim 10^{3.3}\,{\rm M}_\odot$.

On the other hand, all runs with stellar winds in addition to SNe show a qualitatively different trend. The most massive clusters grow on the shortest time-scales $\sim 10^4$ yr, much shorter than the shortest stellar lifetimes. Here, the winds from the forming massive stars efficiently clear out the local environments and thus, terminate the gas accretion on to the cluster. This process is more efficient for more massive clusters and we see a clear anticorrelation between cluster formation time and cluster mass, ranging from $\sim 10^6$ yr for clusters with $M_{\rm sink,\,max} \sim 10^{2.7}\,{\rm M}_\odot$ to $\sim 10^4$ yr for $M_{\rm sink,\,max} \sim 10^4\,{\rm M}_\odot$. We note that the quoted values for the cluster accretion times are most likely underestimates, since we do not consider the dynamical evolution of gas within the sink particle. The typical accretion rates on to the cluster sinks are $10^{-3}$–$10^{-2}\,{\rm M}_\odot\,{\rm yr}^{-1}$. In the case of winds, this is only valid within approximately the first Myr. The logarithmic mean of $t_{\rm sink,\,max}$ is also given in Table 2. All our models with stellar feedback are in agreement with the idea of the rapid removal of gas from the clusters on time-scales $\lesssim$10–30 Myr, which is observed in star clusters in the Milky Way (Lada & Lada 2003; see also de Grijs 2010 and references therein for a summary). In this regard, we conform with recent observational findings that young clusters are gas free within 2–3 Myr and thus, that the formation time-scale of clusters is short (see the review by Longmore et al. 2014). This has been found for relatively low-mass clusters ($\sim 10^3\,{\rm M}_\odot$; e.g. Seale et al. 2012), intermediate-mass clusters ($\sim 10^4$–$10^5\,{\rm M}_\odot$; e.g. Hollyhead et al. 2015), and even the highest mass clusters ($>10^6\,{\rm M}_\odot$; Bastian, Hollyhead & Cabrera-Ziri 2014).

We conclude that stellar winds regulate the accretion of gas on to the forming star-cluster sink right after the first massive star(s) have been born, while SNe explode only late (after $\gtrsim$5 Myr) and fail to regulate accretion in a way to produce enough lower mass clusters.

## 5 HOW SUPERNOVA FEEDBACK DRIVES GALACTIC OUTFLOWS

The impact of the SN explosions on the ISM depends on the structure and the density of the gas near the explosion centre (see

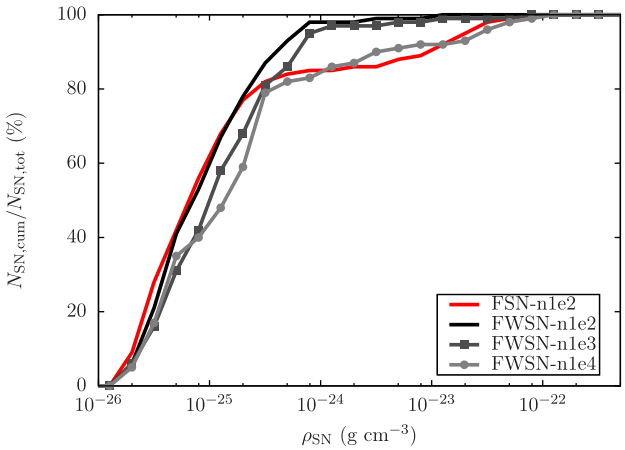


**Figure 11.** Normalized cumulative distribution of SNe as a function of the mean environmental gas density (in the region where the SN explodes), $\rho_{\rm SN}$, for all simulations with SNe. For high-enough SFRs, the stellar wind feedback clears out the SN environment before their explosion resulting in typical environmental densities of $\sim 10^{-25}\,{\rm g\,cm^{-3}}$. But even the clustering of massive stars and their SNe alone is sufficient to have 80 per cent of all SNe explode in environments with reduced density.

e.g. Iffrig & Hennebelle 2015; Kim & Ostriker 2015a; Martizzi, Faucher-Giguère & Quataert 2015; Walch & Naab 2015; Wareing, Pittard & Falle 2016, for recent high-resolution numerical simulations). SNe exploding in high-density environments are subject to rapid radiative cooling and do not inject large amounts of radial momentum (see Haid et al. 2016; Hu et al. 2016, for studies of the momentum injection of SNe in different environments). The average SN rate per Myr in each simulation, $\dot{N}_{\rm SN}$, is listed in Table 2.

We probe the mean density in each SN injection region, $\rho_{\rm SN}$, to understand which ambient conditions the SN explosions encounter in the different simulations. This is depicted in Fig. 11, where we plot the cumulative distribution of all SNe as a function of $\rho_{\rm SN}$. We find that in run FSN-n1e2 with only SN feedback, ∼80 per cent of all SNe explode in relatively low-density gas with $\rho \sim 10^{-25}\,{\rm g\,cm^{-3}}$

and only ∼15 per cent explode in higher density gas with $\rho \gtrsim 10^{-23}$ g cm$^{-3}$. The reason is the clustering of the massive stars and hence of the SN feedback. Only the first SN in a cluster interacts with a denser environment, while the following ones explode inside the low-density bubble (Mac Low & McCray 1988; Chu & Mac Low 1990). Clustering can also lead to the formation of super bubbles (Wünsch et al. 2008). With wind feedback included, basically all SN environments are reduced in density before the first explosion. Only run FWSN-n1e3, which has a much lower SFR, also has a small fraction of SNe that interact with dense gas.

Observations of OH maser emission also identify that ∼10 per cent of all SN remnants in the Milky Way are interacting with dense gas (Hewitt & Yusef-Zadeh 2009). Furthermore, Elwood, Murphy & Diaz (2016) have studied the distribution of environmental densities for SN remnants in M31 and M33. They derive a narrow lognormal distribution of environmental densities with a mean number density of $\bar{n}_{\rm SN} = 0.07$ cm$^{-3}$ and a standard deviation of $\sigma_{\rm SN} = 0.7$. To compare with the observed results, we fit a lognormal distribution for the environmental densities of the two runs that can be fitted with a single component. The following values give the best fit to the respective distribution.

(i) For run FWSN-n1e2, we find a mean density of $\sim 8 \times 10^{-26}$ g cm$^{-3}$, which corresponds to $\bar{n}_{\rm SN} \approx 0.07$ cm$^{-3}$, and a standard deviation of $\sigma_{\rm SN} = 0.9$.
(ii) For run FWSN-n1e3, we find a mean density of $\sim 10^{-25}$ g cm$^{-3}$, which corresponds to $\bar{n}_{\rm SN} \approx 0.09$ cm$^{-3}$, and a standard deviation of $\sigma_{\rm SN} = 1.1$.

Overall, the SN remnants in the simulations presented here encounter low-density environments, and are therefore well resolved. In this case, thermal energy input can be safely used without the problem of numerical overcooling (Gatto et al. 2015).

We define gas as *hot gas* if it has a temperature $T > 3 \times 10^5$ K. This gas is in the *thermally stable*, hot phase (Dalgarno & McCray 1972). In the following we show that, in case enough SNe explode in low-density environments, a hot, volume-filling phase is developed (see e.g. Gatto et al. 2015; Li et al. 2015, for this process in regions with periodic boundaries) and galactic outflows can be launched. In the upper panel of Fig. 12, we plot the time evolution of the hot gas VFF within $z = \pm 100$ pc around the disc mid-plane. The cyan triangles mark the time of the formation of the first cluster plus 20 Myr ($t_{\rm sink,\,20} = t_{\rm sink,\,0} + 20$ Myr). At this point, feedback from the first massive stars had enough time to change the structure of the surrounding ISM. All runs with SN feedback and high SFRs (runs FSN-n1e2, FWSN-n1e2, and FWSN-n1e3) develop volume-filling hot gas with VFF $\gtrsim 50$ per cent at $t_{\rm sink,\,20}$ and more than 80 per cent towards $t_{\rm stop}$. Run NoF-n1e2 also seems to have a fairly high hot gas VFF, but this is caused by the collapse of the disc into a thin sheet and the accretion of most of the gas into sink particles. However, run FW-n1e2 without SN feedback and run FWSN-1e4, which has a SFR surface density that is below the KS relation, do not form a hot volume-filling phase and the hot gas VFF stays below 40 per cent after $t_{\rm sink,\,20}$.

In total, we define four temperature regimes (see Paper I) –

(i) hot: $T > 3 \times 10^5$ K,
(ii) warm–hot: $8000 < T \leq 3 \times 10^5$ K,
(iii) warm: $300 < T \leq 8000$ K,
(iv) cold: $30 < T \leq 300$ K.

For completeness, the evolution of warm–hot, warm, and cold gas is shown in Fig. B2 (see Appendix B).

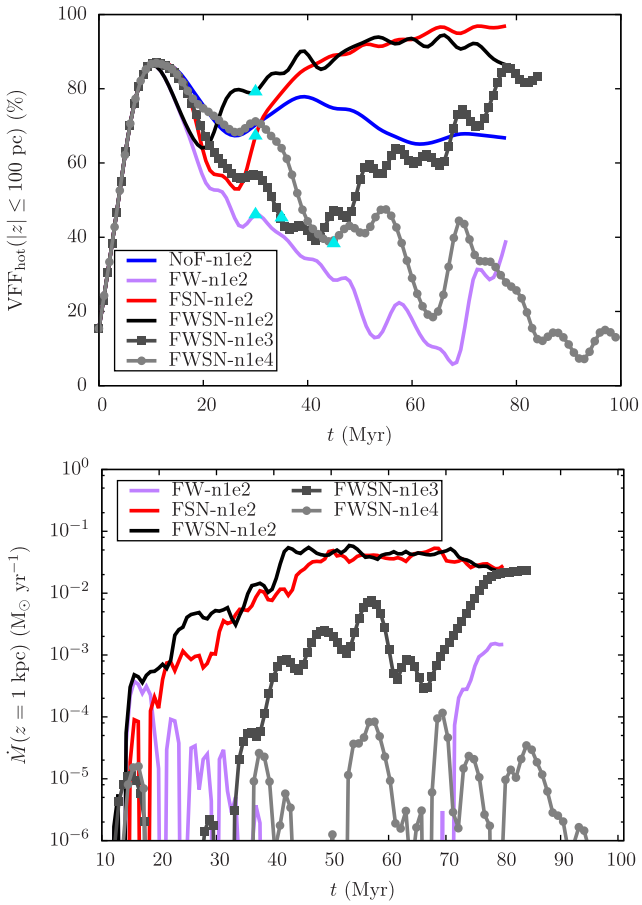


**Figure 12.** Top: time evolution of the hot gas VFFs (all gas with $T > 3 \times 10^5$ K) within $z = \pm 100$ pc around the disc mid-plane. The cyan triangles show the time from which onwards we compute the mass-loading factors for each run as shown in Fig. 13, which corresponds to $t_{\rm sink,\,20} = t_{\rm sink,\,0} + 20$ Myr. Bottom: time evolution of the total gas outflow rates at 1 kpc above and below the disc mid-plane. Only simulations with high-enough SN rates (FSN-n1e2, FWSN-n1e2, FWSN-n1e3) develop high VFFs of hot gas and significant outflows.

Furthermore, we show the time evolution of the total outflowing gas mass through surfaces at $z = \pm 1$ kpc in the lower panel of Fig. 12. All runs with a hot volume-filling phase also have relatively high outflow rates of $\dot{M}(z = \pm 1\ {\rm kpc}) \gtrsim 2 \times 10^{-2}$ M$_\odot$ yr$^{-1}$ at $t_{\rm stop}$. The two runs with a low hot gas VFF also have significantly lower outflow rates.

A better quantity to define the efficiency of galactic outflows that are driven by thermal pressure is the so-called *mass-loading factor*, which is defined as the total gas outflow rate surface density, $\Sigma_{\rm OFR}$ in [M$_\odot$ yr$^{-1}$ kpc$^{-2}$], over the SFR surface density. We note that this quantity only becomes meaningful in combination with the distance (from the star formation event) where the outflow rate is measured. We correlate the hot gas VFF and the mass-loading factor in Fig. 13. Each point represents the average over a time bin of $\Delta t = 1$ Myr as calculated for all times starting from $t_{\rm sink,\,20}$ up to $t_{\rm stop}$. The dotted horizontal line indicates a mass-loading factor of 1, and the dotted vertical line shows the VFF of 50 per cent. There is a very clear trend that simulations with hot gas VFFs that are higher than 50 per cent have mass-loading factors above 1, while the two runs with low hot gas VFFs (run FW-n1e2 and run FWSN-n1e4) also have

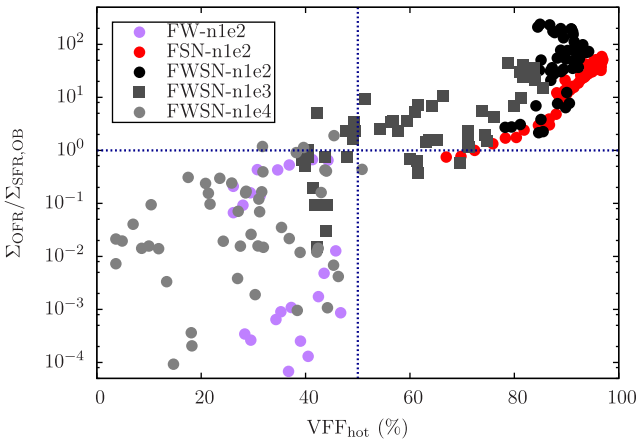


**Figure 13.** Mass loading, measured from the ratio of the surface density of the outflowing gas at $z = \pm 1$ kpc and the SFR surface density, as a function of the hot gas VFF within $\pm 100$ pc for all simulations with feedback (the run without feedback does not develop any outflows and is therefore not shown). The data is binned in time with $\Delta t = 1$ Myr. Only simulations with a hot gas filling fraction of more than $\sim$50 per cent, which has been created due to SN feedback, are associated with outflows with mass loading $\gtrsim 1$ (as indicated by the dotted, dark-blue lines).

mass-loading factors smaller than 1. The runs with low mass loading and low hot gas VFF actually have some points missing where there is no outflow at all. This is also the case for run NoF-n1e2, which has a mass-loading factor equal to zero at all times. While there seems to be an exponential correlation above for the high mass-loading factors, there is a large scatter for low mass-loading factors and therefore we do not provide fits to the distributions.

In summary, we clearly find that outflows from the galactic disc can be launched by the thermal pressure of the SN-driven, hot gas, in cases where the SFR (i.e. the SN rate) is high enough to cause a hot volume filling phase (see Girichidis et al. 2016b, for wind-launching mechanisms driven by non-thermal cosmic rays). Simulations with stellar winds alone fail to produce significant outflows.

This is in qualitative agreement with investigations by Gatto et al. (2015) and Li et al. (2015) who study the SN-driven ISM in periodic set-ups. They show that the thermal pressure becomes very high in cases where the SNe can drive the hot gas VFF above 50 per cent. In periodic set-ups, where the gas is confined and the pressure cannot be released by outflows, this leads to a thermal runaway, where most of the gas mass is compressed into small clumps and most of the volume is filled with hot gas. A high hot gas VFF is reached for high-enough SN rates, in which case the bubbles start to overlap.

## 6 CONCLUSIONS

We study the impact of stellar winds and SNe on the multiphase ISM in a representative piece of a galactic disc with $\Sigma_{\rm gas} = 10\,{\rm M}_\odot\,{\rm pc}^{-2}$ and a size of $(500\,{\rm pc})^2 \times \pm 5\,{\rm kpc}$. We include an external, static, stellar potential as well as gas self-gravity, radiative cooling and diffuse heating, sink particles and stellar feedback in the form of stellar winds and SN explosions. We take into account dust and gas (self-) shielding and we track the distribution of molecular gas using a chemical network that allows us to follow the formation, evolution, and destruction of H, $H^+$, $H_2$, CO, $C^+$.

Star formation is modelled via cluster-sink particles, which are allowed to accrete throughout the simulation. We implement a sub-grid model for the feedback from massive stars, where we randomly sample massive stars from the IMF and follow the wind feedback of each single massive star using the latest Geneva stellar tracks. The injected wind luminosity corresponds to the total wind luminosity of all massive stars in the cluster. At the end of their lifetime the stars undergo a Type II SN explosion. We switch on and off wind and SN feedback to study how each feedback mechanism affects the multiphase ISM structure.

We find the following.

(i) For a given stellar population, the energy injected by stellar winds is mostly dominated by short-lived very high-mass stars, while the majority of the energy injected as SNe comes from long-lived progenitors with lower masses. Compared to stellar winds, SNe dominate the total injected energy, but only by a factor of $\sim$3.

(ii) Models with stellar winds and SNe show the best agreement with observations of nearby *normal* star-forming galaxies.

(iii) Stellar winds regulate the growth of young cluster sinks by quenching the gas accretion on to them shortly after the first massive star has been born. SN feedback is significantly delayed and thus, allows for longer time-scales of efficient gas accretion (up to the first SN explosion after $\sim$5 Myr). Stellar winds qualitatively change cluster formation time-scales. More massive clusters have shorter formation time-scales. In simulations without winds, such an anticorrelation does not exist.

(iv) Strong shock-heating by SN explosions and possibly overlapping SN remnants creates a hot volume-filling gas phase near the disc mid-plane. Stellar winds are less energetic and convert most of the cold and warm gas into a warm and warm–hot gas.

(v) Thermal pressure of the hot gas can drive outflows with significant mass-loading factors as measured at $z = \pm 1$ kpc. This is possible if the SFR and hence the SN rate in the discs is high enough to produce a hot gas VFF of more than $\sim$50 per cent.

## ACKNOWLEDGEMENTS

The SILCC project details are available at http://www.astro.uni-koeln.de/silcc. All simulations have been performed on the Odin and Hydra clusters hosted by the Max Planck Computing & Data Facility (http://www.mpcdf.mpg.de/). We thank M. Anderson, C. Federrath, J. Mackey, M. M. Mac Low, E. Pellegrini, and X. Shi for useful discussions and Leroy et al. (2008) and Ekström et al. (2012) for making their data publicly available. AG, SW, TN, PG, SCOG, RSK, and TP acknowledge the Deutsche Forschungsgemeinschaft (DFG) for funding through the SPP 1573 'The Physics of the Interstellar Medium'. SW acknowledges funding by the Bonn-Cologne-Graduate School, by SFB 956 'The conditions and impact of star formation', and from the European Research Council under the European Community's Framework Programme FP8 via the ERC Starting Grant RADFEEDBACK (project number 679852). TN acknowledges support by the DFG cluster of excellence 'Origin and Structure of the Universe'. RW acknowledges support by the Czech Science Foundation project 15-06012S and by the institutional project RVO: 67985815. RSK and SCOG acknowledge support from the DFG via SFB 881 'The Milky Way System' (sub-projects B1, B2, and B8). RSK acknowledges support from the European Research Council under the European Community's Seventh Framework Programme (FP7/2007-2013) via the ERC Advanced Grant STARLIGHT (project number 339177). The software used in this work was in part developed by the DOE NNSA-ASC OASCR Flash Center at the University of Chicago. We thank

C. Karch for the program package FY and M. Turk and the YT community for the YT project (Turk et al. 2011).

## REFERENCES


Agertz O., Kravtsov A. V., Leitner S. N., Gnedin N. Y., 2013, ApJ, 770, 25
Bastian N., Hollyhead K., Cabrera-Ziri I., 2014, MNRAS, 445, 378
Bate M. R., Bonnell I. A., Price N. M., 1995, MNRAS, 277, 362
Bleuler A., Teyssier R., 2014, MNRAS, 445, 4015
Bouchut F., Klingenberg C., Waagan K., 2007, Numer. Math., 108, 7
Bouchut F., Klingenberg C., Waagan K., 2010, Numer. Math., 115, 647
Caldú-Primo A., Schruba A., Walter F., Leroy A., Sandstrom K., de Blok W. J. G., Ianjamasimanana R., Mogotsi K. M., 2013, AJ, 146, 150
Chabrier G., 2003, PASP, 115, 763
Chu Y.-H., Mac Low M.-M., 1990, ApJ, 365, 510
Clark P. C., Glover S. C. O., Klessen R. S., 2012, MNRAS, 420, 745
Cox D. P., Smith B. W., 1974, ApJ, 189, L105
Creasey P., Theuns T., Bower R. G., 2013, MNRAS, 429, 1922
Crowther P. A., 2007, ARA&A, 45, 177
Dale J. E., Ercolano B., Bonnell I. A., 2012, MNRAS, 424, 377
Dale J. E., Ngoumou J., Ercolano B., Bonnell I. A., 2014, MNRAS, 442, 694
Dalgarno A., McCray R. A., 1972, ARA&A, 10, 375
de Avillez M. A., Breitschwerdt D., 2004, A&A, 425, 899
de Avillez M. A., Breitschwerdt D., 2007, ApJ, 665, L35
de Grijs R., 2010, Phil. Trans. R. Soc. A, 368, 693
de Grijs R., Anders P., Bastian N., Lynds R., Lamers H. J. G. L. M., O'Neil E. J., 2003, MNRAS, 343, 1285
Dib S., Bell E., Burkert A., 2006, ApJ, 638, 797
Dobbs C. L., Pringle J. E., 2013, MNRAS, 432, 653
Doran E. I. et al., 2013, A&A, 558, A134
Draine B. T., 1978, ApJS, 36, 595
Dubey A. et al., 2008, in Pogorelov N. V., Audit E., Zank G. P., eds, ASP Conf. Ser. Vol. 385, Numerical Modeling of Space Plasma Flows. Astron. Soc. Pac., San Francisco, p. 145
Dubey A. et al., 2013, Int. J. High Perform. Comput. Appl., 551, L105
Ekström S. et al., 2012, A&A, 537, A146
Elwood B., Murphy J., Diaz M., 2016, Am. Astron. Soc. Meeting Abstracts, 227, 302.07
Eswaran V., Pope S., 1988, Comput. Fluids, 16, 257
Federrath C., Banerjee R., Clark P. C., Klessen R. S., 2010, ApJ, 713, 269
Ferrière K. M., 2001, Rev. Mod. Phys., 73, 1031
Fryxell B. et al., 2000, ApJS, 131, 273
Fujii M. S., Portegies Zwart S., 2016, ApJ, 817, 4
Gatto A. et al., 2015, MNRAS, 449, 1057
Geen S., Rosdahl J., Blaizot J., Devriendt J., Slyz A., 2015, MNRAS, 448, 3248
Gent F. A., Shukurov A., Sarson G. R., Fletcher A., Mantere M. J., 2013a, MNRAS, 430, L40
Gent F. A., Shukurov A., Fletcher A., Sarson G. R., Mantere M. J., 2013b, MNRAS, 432, 1396
Genzel R. et al., 2010, MNRAS, 407, 2091
Georgy C., Ekström S., Meynet G., Massey P., Levesque E. M., Hirschi R., Eggenberger P., Maeder A., 2012, A&A, 542, A29
Gieles M., Larsen S. S., Bastian N., Stein I. T., 2006, A&A, 450, 129
Girichidis P. et al., 2016a, MNRAS, 456, 3432 ( Paper II)
Girichidis P. et al., 2016b, ApJ, 816, L19
Glover S. C. O., Clark P. C., 2012, MNRAS, 421, 116
Glover S. C. O., Mac Low M.-M., 2007a, ApJS, 169, 239
Glover S. C. O., Mac Low M.-M., 2007b, ApJ, 659, 1317
Glover S. C. O., Federrath C., Mac Low M.-M., Klessen R. S., 2010, MNRAS, 404, 2
Gnat O., Ferland G. J., 2012, ApJS, 199, 20
Goodman A. A., Barranco J. A., Wilner D. J., Heyer M. H., 1998, ApJ, 504, 223
Gräfener G., Hamann W.-R., 2008, A&A, 482, 945
Habing H. J., 1968, Bull. Astron. Inst. Neth., 19, 421
Haid S., Walch S., Naab T., Seifried D., Mackey J., Gatto A., 2016, MNRAS, 460, 2962
Heiles C., Troland T. H., 2003, ApJ, 586, 1067
Heitsch F., Mac Low M.-M., Klessen R. S., 2001, ApJ, 547, 280
Hennebelle P., Iffrig O., 2014, A&A, 570, A81
Hewitt J. W., Yusef-Zadeh F., 2009, ApJ, 694, L16
Hill A. S., Joung M. R., Mac Low M.-M., Benjamin R. A., Haffner L. M., Klingenberg C., Waagan K., 2012, ApJ, 750, 104
Hollyhead K., Bastian N., Adamo A., Silva-Villa E., Dale J., Ryon J. E., Gazak Z., 2015, MNRAS, 449, 1106
Hopkins P. F., Kereš D., Oñorbe J., Faucher-Giguère C.-A., Quataert E., Murray N., Bullock J. S., 2014, MNRAS, 445, 581
Hu C.-Y., Naab T., Walch S., Glover S. C. O., Clark P. C., 2016, MNRAS, 458, 3528
Hubber D. A., Walch S., Whitworth A. P., 2013, MNRAS, 430, 3261
Ianjamasimanana R., de Blok W. J. G., Walter F., Heald G. H., Caldú-Primo A., Jarrett T. H., 2015, AJ, 150, 47
Iffrig O., Hennebelle P., 2015, A&A, 576, A95
Jappsen A.-K., Klessen R. S., Larson R. B., Li Y., Mac Low M.-M., 2005, A&A, 435, 611
Joung M. K. R., Mac Low M.-M., 2006, ApJ, 653, 1266
Joung M. R., Mac Low M.-M., Bryan G. L., 2009, ApJ, 704, 137
Kalberla P. M. W., Dedes L., 2008, A&A, 487, 951
Kennicutt R. C., Jr, 1998, ApJ, 498, 541
Kim C.-G., Ostriker E. C., 2015a, ApJ, 802, 99
Kim C.-G., Ostriker E. C., 2015b, ApJ, 815, 67
Kim C.-G., Ostriker E. C., Kim W.-T., 2013, ApJ, 776, 1
Klessen R. S., Glover S. C. O., 2016, Saas-Fee Advanced Course, Volume 43, Star Formation in Galaxy Evolution: Connecting Numerical Models to Reality. Springer-Verlag, Berlin, p. 85
Klassen M., Pudritz R., Kuiper R., Peters T., Banerjee R., 2016, ApJ, 823, 28
Kroupa P., 2001, MNRAS, 322, 231
Kroupa P., 2002, Science, 295, 82
Krtička J., 2006, MNRAS, 367, 1282
Krumholz M. R., Matzner C. D., 2009, ApJ, 703, 1352
Krumholz M. R., Thompson T. A., 2012, ApJ, 760, 155
Krumholz M. R., McKee C. F., Klein R. I., 2004, ApJ, 611, 399
Kudritzki R.-P., Puls J., 2000, ARA&A, 38, 613
Kudritzki R. P., Pauldrach A., Puls J., 1987, A&A, 173, 293
Lada C. J., Lada E. A., 2003, ARA&A, 41, 57
Larson R. B., 1981, MNRAS, 194, 809
Leitherer C., Robert C., Drissen L., 1992, ApJ, 401, 596
Leroy A. K., Walter F., Brinks E., Bigiel F., de Blok W. J. G., Madore B., Thornley M. D., 2008, AJ, 136, 2782
Li M., Ostriker J. P., Cen R., Bryan G. L., Naab T., 2015, ApJ, 814, 4
Longmore S. N. et al., 2014, in Beuther H., Klessen R. S., Dullemond C. P., Henning T., eds, Protostars and Planets VI. Univ. Arizona Press, Tucson, AZ, p. 291
Mac Low M.-M., Klessen R. S., 2004, Rev. Mod. Phys., 76, 125
Mac Low M.-M., McCray R., 1988, ApJ, 324, 776
Mac Low M.-M., Balsara D. S., Kim J., de Avillez M. A., 2005, ApJ, 626, 864
McKee C. F., Ostriker J. P., 1977, ApJ, 218, 148
Mackey J., Gvaramadze V. V., Mohamed S., Langer N., 2015, A&A, 573, A10
Marinacci F., Pakmor R., Springel V., Simpson C. M., 2014, MNRAS, 442, 3745
Markova N., Puls J., 2008, A&A, 478, 823
Martizzi D., Faucher-Giguère C.-A., Quataert E., 2015, MNRAS, 450, 504
Mokiem M. R. et al., 2007, A&A, 473, 603
Murray N., Quataert E., Thompson T. A., 2010, ApJ, 709, 191
Nelson R. P., Langer W. D., 1997, ApJ, 482, 796
Oppenheimer B. D., Davé R., Kereš D., Fardal M., Katz N., Kollmeier J. A., Weinberg D. H., 2010, MNRAS, 406, 2325
Ostriker E. C., McKee C. F., Leroy A. K., 2010, ApJ, 721, 975
Pellegrini E. W., Baldwin J. A., Ferland G. J., 2011, ApJ, 738, 34

Peters T., Banerjee R., Klessen R. S., Mac Low M.-M., Galván-Madrid R., Keto E. R., 2010, ApJ, 711, 1017
Peters T., Banerjee R., Klessen R. S., Mac Low M.-M., 2011, ApJ, 729, 72
Peters T. et al., 2015, ApJ, 813, L27
Petric A. O., Rupen M. P., 2007, AJ, 134, 1952
Piskunov A. E., Kharchenko N. V., Schilbach E., Röser S., Scholz R.-D., Zinnecker H., 2008, A&A, 487, 557
Puls J., Vink J. S., Najarro F., 2008, A&AR, 16, 209
Rogers H., Pittard J. M., 2013, MNRAS, 431, 1337
Salpeter E. E., 1955, ApJ, 121, 161
Seale J. P., Looney L. W., Wong T., Ott J., Klein U., Pineda J. L., 2012, ApJ, 751, 42
Sembach K. R., Howk J. C., Ryans R. S. I., Keenan F. P., 2000, ApJ, 528, 310
Shetty R., Ostriker E. C., 2012, ApJ, 754, 2
Slyz A. D., Devriendt J. E. G., Bryan G., Silk J., 2005, MNRAS, 356, 737
Somerville R. S., Davé R., 2015, ARA&A, 53, 51
Spitzer L., Jr, 1942, ApJ, 95, 329
Tacconi L. J. et al., 2013, ApJ, 768, 74
Tamburro D., Rix H.-W., Leroy A. K., Mac Low M.-M., Walter F., Kennicutt R. C., Brinks E., de Blok W. J. G., 2009, AJ, 137, 4424
Toalá J. A., Arthur S. J., 2011, ApJ, 737, 100
Truelove J. K., Klein R. I., McKee C. F., Holliman J. H., II, Howell L. H., Greenough J. A., 1997, ApJ, 489, L179
Turk M. J., Smith B. D., Oishi J. S., Skory S., Skillman S. W., Abel T., Norman M. L., 2011, ApJS, 192, 9
van Loon J. T., 2006, in Lamers H. J. G. L. M., Langer N., Nugis T., Annuk K., eds, ASP Conf. Ser. Vol. 353, Stellar Evolution at Low Metallicity: Mass Loss, Explosions, Cosmology. Astron. Soc. Pac., San Francisco, p. 211
Vink J. S., de Koter A., Lamers H. J. G. L. M., 2001, A&A, 369, 574
Waagan K., 2009, J. Comput. Phys., 228, 8609
Waagan K., Federrath C., Klingenberg C., 2011, J. Comput. Phys., 230, 3331
Walch S., Naab T., 2015, MNRAS, 451, 2757
Walch S. K., Whitworth A. P., Bisbas T., Wünsch R., Hubber D., 2012, MNRAS, 427, 625
Walch S., Whitworth A. P., Bisbas T. G., Wünsch R., Hubber D. A., 2013, MNRAS, 435, 917
Walch S. et al., 2015, MNRAS, 454, 238 ( Paper I)
Wareing C. J., Pittard J. M., Falle S. A. E. G., 2016, preprint (arXiv:1605.04706)
Wolfire M. G., Hollenbach D., McKee C. F., Tielens A. G. G. M., Bakes E. L. O., 1995, ApJ, 443, 152
Wünsch R., Tenorio-Tagle G., Palouš J., Silich S., 2008, ApJ, 683, 683
Wünsch R., Silich S., Palouš J., Tenorio-Tagle G., Muñoz-Tuñón C., 2011, ApJ, 740, 75
Zuckerman B., Evans N. J., II1974, ApJ, 192, L149

## APPENDIX A: SIMULATION SNAPSHOTS

In Figs A1–A3, we show snapshots of simulations NoF-n1e2 and FW-n1e2 (Fig. A1), FSN-n1e2 and FWSN-n1e2 (Fig. A2), and FWSN-n1e4 (Fig. A3) at $\sim t_{\mathrm{sink},\,0} + 31$ Myr. As described in Section 3 for Fig. 2, the different panels show (from left to right) a slice of the total density and of the gas temperature at $y = 0$ (top) and at $z = 0$ (bottom), the total gas column density, and the column densities of $H^+$, H, and $H_2$. The location of the cluster-sink particles is indicated by the small white circles.

Runs with SN feedback show larger disc scaleheights, which is clearly visible in the projections of the total column density or the atomic hydrogen column density. Only run FWSN-n1e4, which has a low SFR, has a smaller scaleheight but more molecular hydrogen.

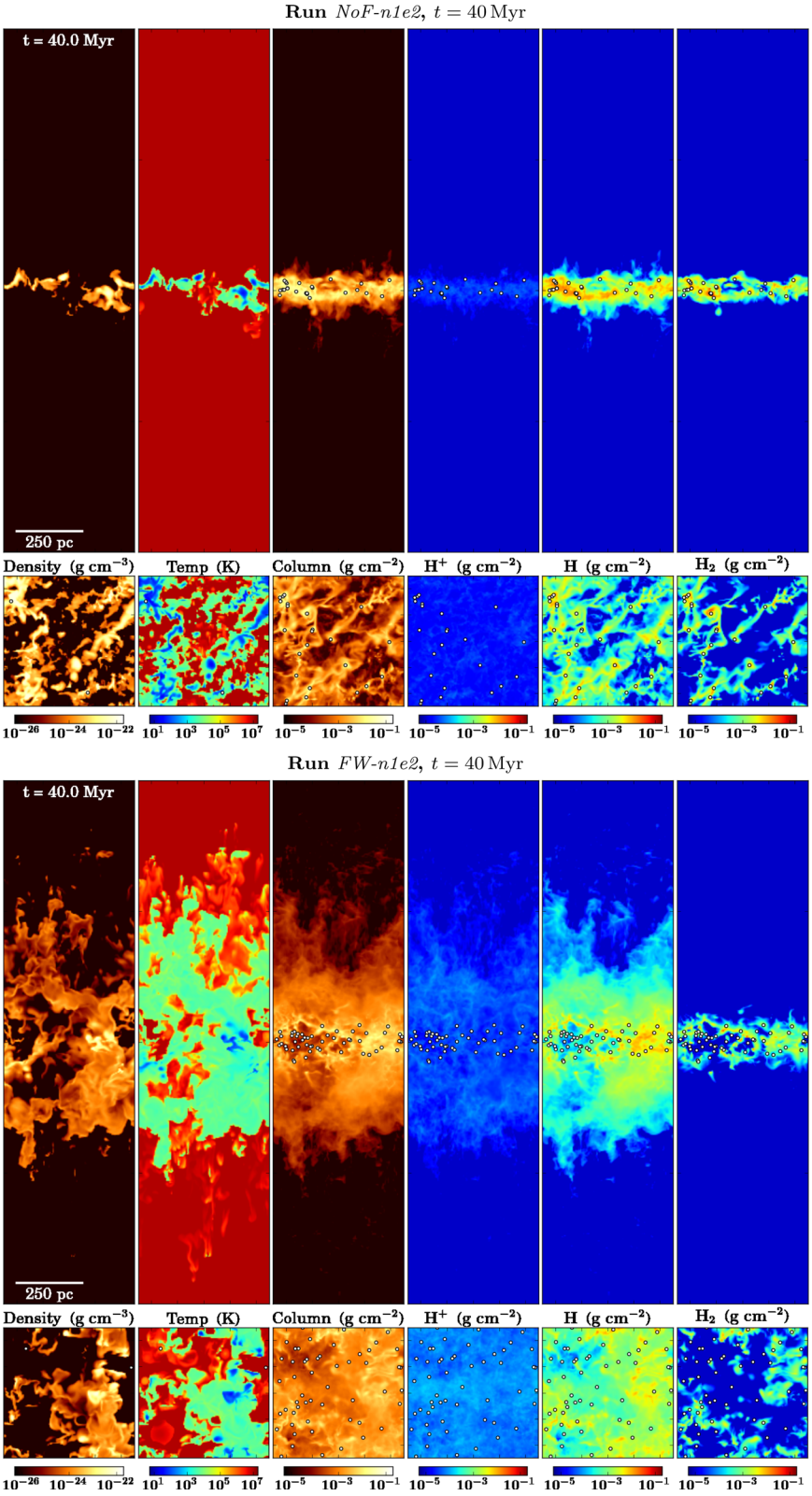


**Figure A1.** Same as Fig. 2 for simulations NoF-n1e2 without feedback from the cluster sinks (top) and run FW-n1e2 with stellar wind feedback (bottom) at $t = 40$ Myr

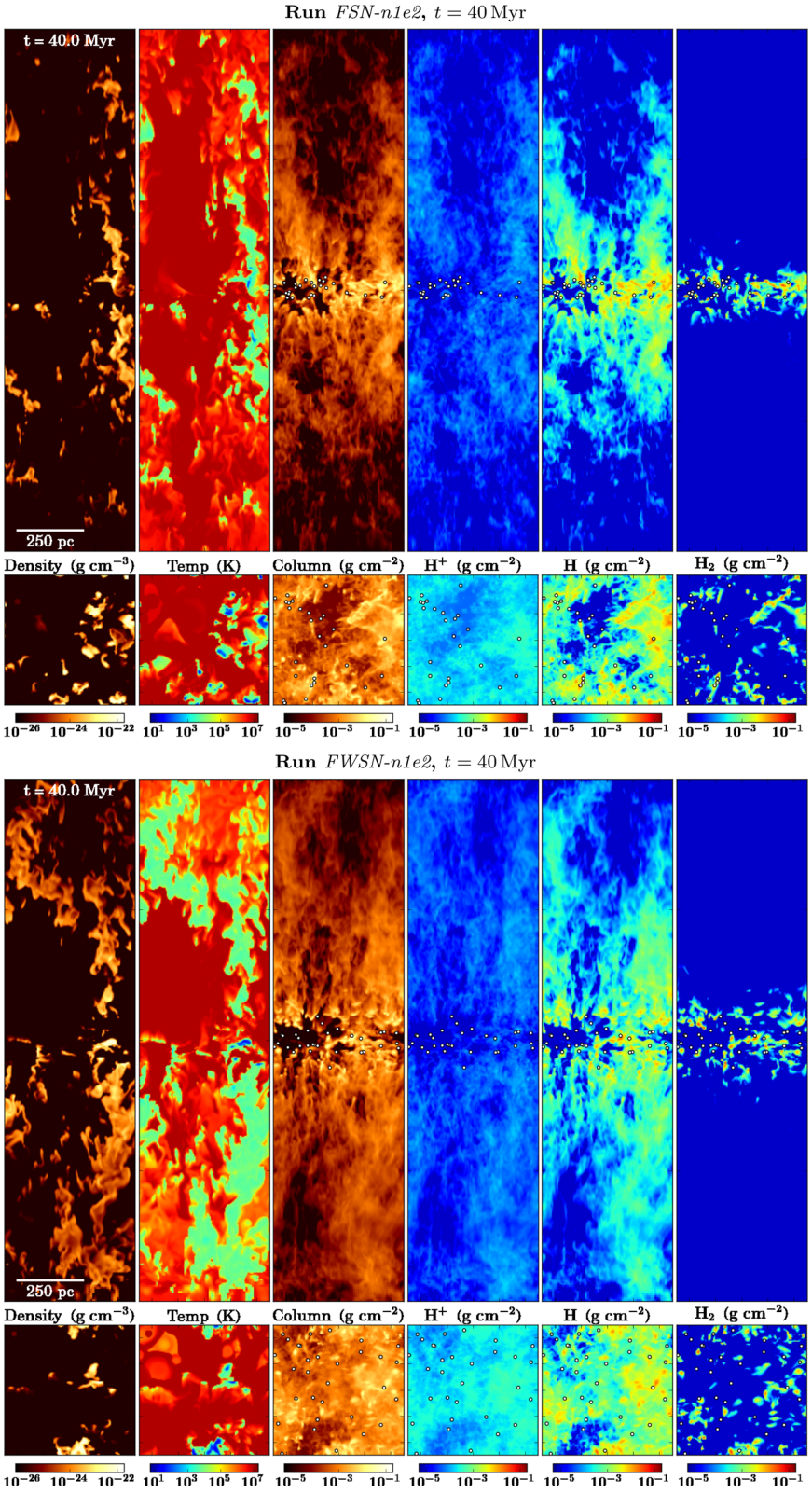


**Figure A2.** Same as Fig. 2 for simulations FSN-n1e2 with SN feedback alone (top) and FWSN-n1e2 with stellar winds and SNe (bottom).

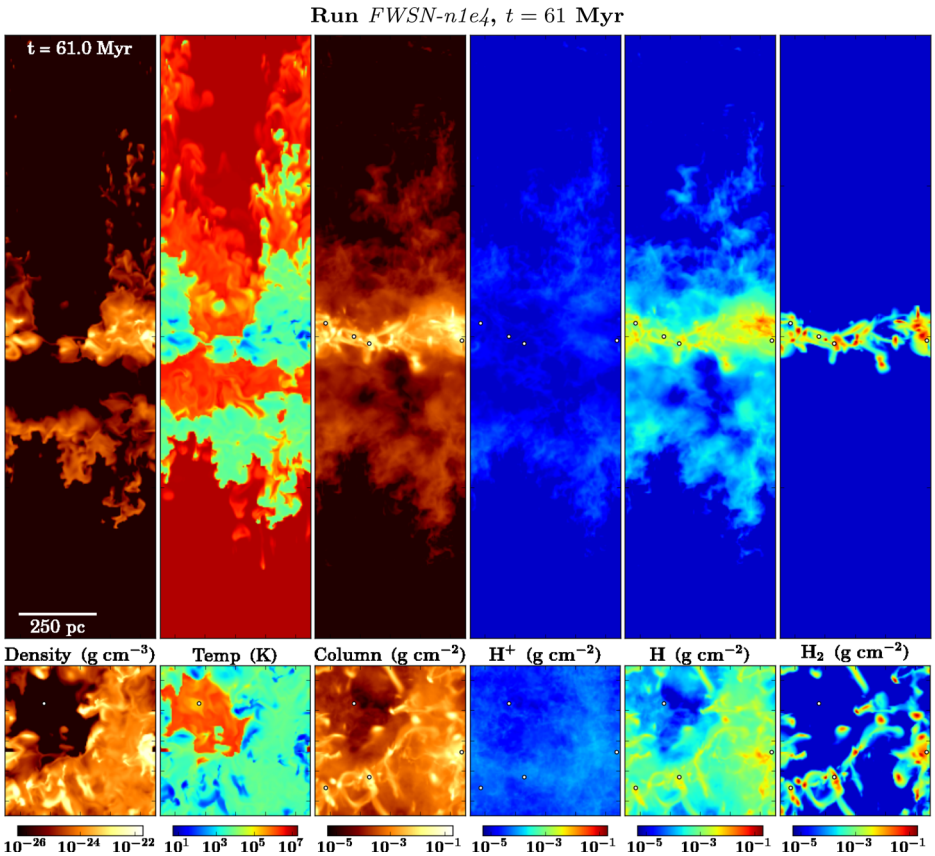


**Figure A3.** Same as Fig. 2 for simulation FWSN-n1e4 at $t = 61$ Myr, where the formation of cluster-sink particles is enabled above $\rho_{\rm sink} = 2 \times 10^{-20}$ g cm$^{-3}$. We show a snapshot at a somewhat later time because the first cluster sink is formed later in these simulations. The higher sink density threshold leads to smaller SFRs and smaller outflow rates (see Fig. 12).

## APPENDIX B: EVOLUTION OF MASS AND VOLUME-FILLING FRACTIONS

In Fig. B1, we show the time evolution of the total gas mass (top-left panel), and of the mass fractions of atomic hydrogen (top right), ionized hydrogen (bottom left), and molecular hydrogen (bottom right), all normalized to the hydrogen gas mass at $t = 0$, $M_0$ (see Section 2.5.2). The total gas mass is complementary to the sink mass evolution. In the run without stellar feedback the SFR is so high (see Fig. 7) that only $\sim 25$ per cent of the total gas mass is left after 80 Myr, while in run FWSN-n1e4 only little mass has collapsed into stars.

At any time most of the hydrogen mass is in atomic form (top-right panel). Overall, runs with a lower SFR have less mass in hot, ionized gas (bottom-left panel) but more mass in atomic and molecular gas (bottom-right panel). We find that SN feedback is needed to produce hot, ionized gas. When comparing the two simulations FW-n1e2 and FWSN-n1e2, which have a very similar evolution of the total gas mass (and of star formation), we find that the latter has significantly more ionized hydrogen but less atomic hydrogen. In addition, run FWSN-n1e4 has a significantly lower SFR than FW-n1e2 but a comparable amount of ionized gas.

For molecular hydrogen (lower right panel), the sink density threshold also plays an important role. For the low sink density threshold, much of the molecular hydrogen gas is accreted on to the sink particles and is assumed to form stars. This leads to an apparently smaller $H_2$ fraction but a larger $M_{\rm sink}$. This result shows that we cannot use runs with $n_{\rm sink} = 10^2 {\rm cm}^{-3}$ to study the $H_2$ content that develops within the galactic disc as most of the dense gas is accreted. For $n_{\rm sink} = 10^4 {\rm cm}^{-3}$, we begin to see similar $H_2$ mass fractions as in runs without sink particles that we presented in Paper I, but the SFR is too low in this simulation. Therefore, the usefulness of runs with cluster-sink particles to study the molecular gas content in a disc galaxy simulation is limited.

In Fig. B2, we show the VFFs of the warm–hot (top), warm (middle), and cold gas (bottom) as a function of time within $z = \pm 100$ pc of the disc mid-plane. The hot gas VFF is shown in Fig. 12. Run FW-n1e2 with stellar wind feedback alone has a low hot gas VFF but therefore a high warm and warm–hot VFF compared to the other simulations with SN feedback, which have a large fraction of the volume filled with hot gas but not much with warm and warm–hot gas. The same applies for run FWSN-n1e4 that has a SN rate that is too low to produce a large hot gas VFF. Also the cold gas VFFs follow this order: runs without SN feedback and/or with a lower SFR are generally colder and have a higher cold gas VFF.

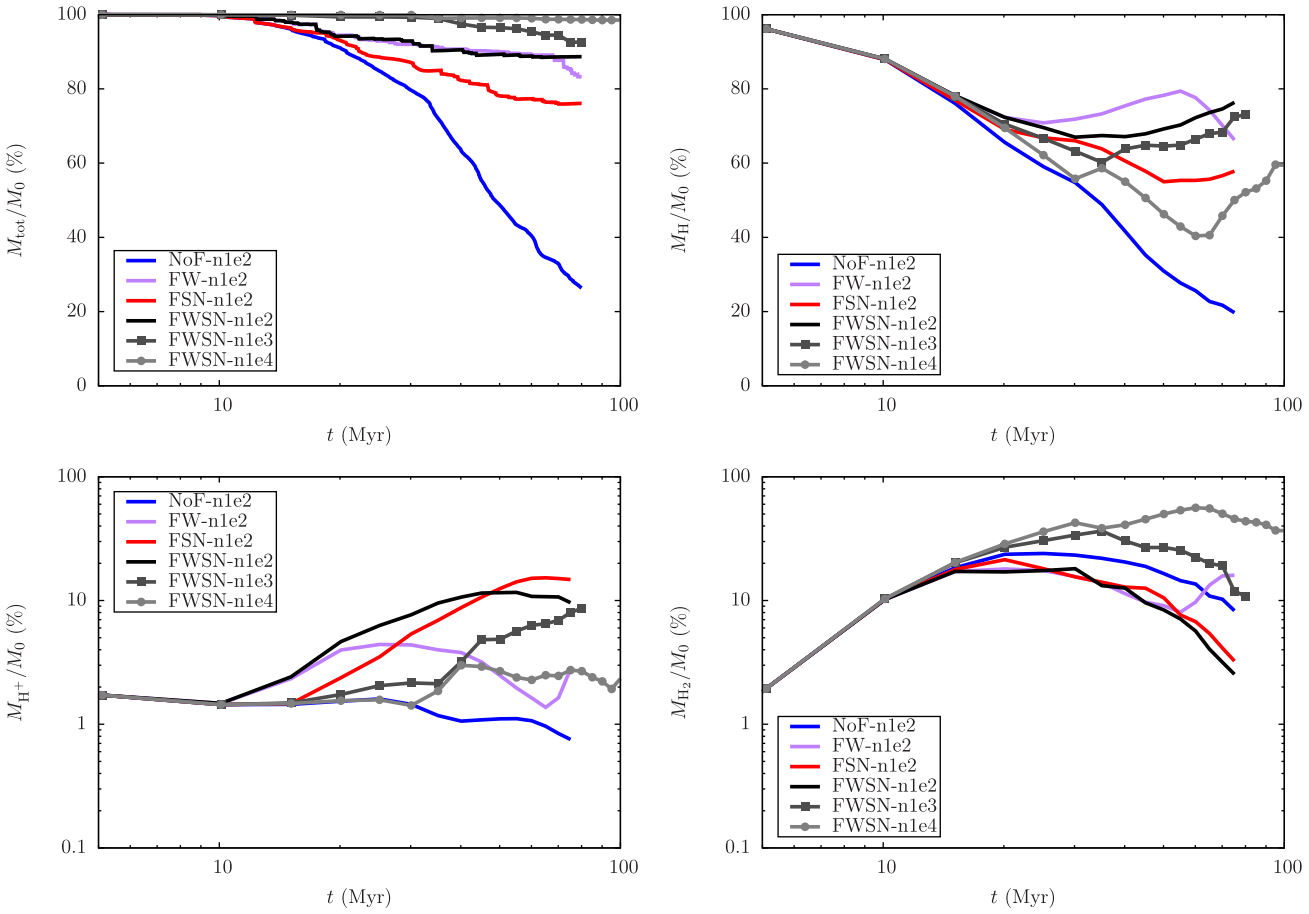


**Figure B1.** Time evolution of the total gas mass (top left), and the mass fractions of atomic hydrogen (top right), ionized hydrogen (bottom left), and molecular hydrogen (bottom right), all normalized to the total mass in hydrogen at $t = 0$. Overall the total gas mass decreases as star formation proceeds. At any time, most of the gas mass is in atomic hydrogen (top-right panel), although we caution that our neglect of radiative feedback from massive stars means that we overproduce warm neutral atomic gas at the expense of warm ionized gas. Most of the hot, ionized gas is caused by SN feedback. For molecular hydrogen, the sink density threshold plays an important role. For the low-density sink threshold, much of the molecular hydrogen gas is accreted on to the sink particles and is assumed to form stars. This leads to an underestimation of the $H_2$ mass fractions in runs with $n_{\rm sink} = 10^2\,{\rm cm}^{-3}$.

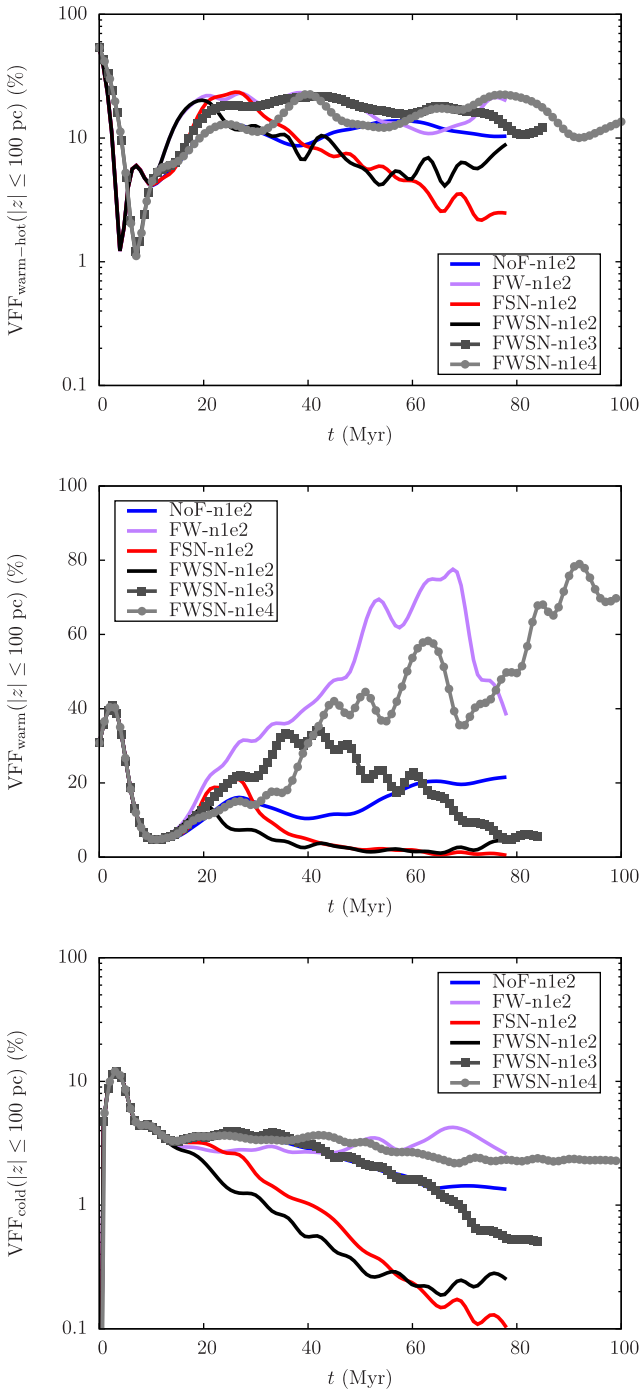


**Figure B2.** Evolution of the VFFs of warm–hot ($8000 < T \leq 3 \times 10^5$ K), warm ($300 < T \leq 8000$ K), and cold gas ($30 < T \leq 300$ K) within $z = \pm 100$ pc from the disc mid-plane.

This paper has been typeset from a TEX/LATEX file prepared by the author.